LA-UR-07-2272

March 14, 2007

Approved for public release;
distribution is unlimited.

Title: Review of the Forest Fire Model

Author(s): R. Menikoff, rtm@lanl.gov
M. Sam Shaw, mss@lanl.gov

Submitted to: Combustion Theory and Modelling

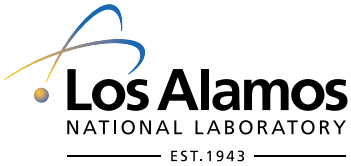

Review of the Forest Fire Model

Ralph Menikoff*
M. Sam Shaw†
Los Alamos National Laboratory

March 14, 2007

Abstract

The Forest Fire burn model is used in reactive hydro simulations to describe both initiation and propagation of a detonation wave. Here we thoroughly review the assumptions of the model, provide a derivation of the Forest fire rate based on characteristics in analogy with Whitham-Chisnell shock dynamics, and discuss issues with code implementation.

1 Introduction

Detonation wave phenomena are simulated using the reactive Euler equations;

$$\frac{\partial}{\partial t}\begin{pmatrix}\rho\\ \rho u\\ \rho E\\ \rho\lambda\end{pmatrix}+\frac{\partial}{\partial x}\begin{pmatrix}\rho u\\ \rho u^2+P\\ \rho u(E+PV)\\ \rho u\lambda\end{pmatrix}=\begin{pmatrix}0\\ 0\\ 0\\ \rho\,\mathcal{R}\end{pmatrix}\ , \tag{1}$$

where ρ is the density, $V=1/\rho$ is the specific volume, $E=e+\frac{1}{2}u^2$ is the total specific energy, e is specific internal energy, u is the particle velocity, P is the pressure, λ is the reaction progress variable and $\mathcal{R}$ is the reaction rate. A high explosive (HE) is assumed to be a mixture of reactants and

*e-mail: rtm@lanl.gov
†e-mail: mss@lanl.gov

products with λ the mass fraction of the products. Moreover, it is assumed that partly burned HE can be characterized by a mixture equation of state (EOS), $P(V, e, \lambda)$, and that the chemical energy is included in e by using a consistent zero of energy for the reactants and the products EOS. Therefore, the EOS accounts for energy released in the reaction and there is no source term in the equation for conservation of energy.

Solid explosives are heterogeneous and have different detonation properties than gaseous and liquid explosives which are homogeneous; see [Campbell et al., 1961a,b]. *Forest fire*[1] is one of the first burn models aimed at describing solid explosives. Though the HE is treated as homogeneous, an "effective" burn rate, rather than a chemical rate, is used to account for reaction due to unresolved hot spots that arise when a heterogeneous explosive is subjected to a strong compressive wave. The model has been widely applied to applications involving initiation and propagation of detonation waves in plastic-bonded explosives (PBX); see [Mader, 1998] and references therein.

The reaction rate for the Forest fire model is assumed to have the form

$$\mathcal{R} = (1 - \lambda)\mathcal{R}_{\mathrm{FF}}(P) \ . \tag{2}$$

The depletion factor, $1-\lambda$, corresponds to a first order reaction. The function $\mathcal{R}_{\mathrm{FF}}(P)$ is fit to shock-to-detonation transition data; see [Mader and Forest, 1976], [Mader, 1998, sec. 4.1]. The purpose of this article is to review the model assumptions, to provide a derivation of the Forest fire rate based on characteristics, and to discuss some of the issues with the implementation and use of the model. Moreover, the Forest fire analysis determines the rate at the shock front needed to fit the shock trajectory from initiation experiments. This rate can be used as a constraint to calibrate parameters for other burn models.

The assumptions of the model are stated and discussed in sec. 2. The reactive shock Hugoniot and Pop-plot data play a key role in the derivation of the Forest fire rate. The reactive locus is described in sec. 3. Typically, the locus is specified by giving the shock velocity as a function of particle velocity. A derivation is given for the burn fraction behind a reactive shock. Next, in sec. 4, the Pop plot and the wedge experiment, on which it is based, are described. Then a derivation of the Forest fire rate, based on characteristics, is presented in sec. 5. In addition, the effect of flow gradients on the rate at

[1]Named after its originator Charles Forest.

the shock front is analyzed. Also an analogy is drawn between the Forest fire analysis and Whitham-Chisnell shock dynamics.

Issues with implementing the Forest fire model in a hydro code are discussed in sec. 6. The most important is the treatment of a reactive shock within the context of a shock capturing algorithm. To illustrate the behavior of the Forest fire model, numerical results for a shock-to-detonation transition are shown in sec. 7. Simplified burn models, such as Forest fire, have generic limitations associated with shock desensitization and the curvature effect. These are briefly discussed in sec. 8. Concluding remarks about homogenization of a PBX and the reaction zone profile of a detonation wave for the Forest fire model are presented in sec. 9.

2 Model assumptions

The Forest fire model has been developed and calibrated for plastic-bonded explosives. These consist of explosive grains held together by a polymeric binder. The cell size for reactive hydro simulations is typically much greater than the size of an average grain. Consequently, a homogenized model is used for the explosive. In addition, a single-step reaction is assumed; reactants to products.

We note that some PBX formulations, such as PBX 9404, use an energetic binder. Moreover, it is known that some explosives, such as TATB, have both fast and slow reactions. Thus, the assumption of a single-step reaction is a crude approximation used to simplify modeling of an HE.[2]

The pressure behind a detonation wave is much higher than the yield strength of the explosive grains. Consequently, for the detonation regime, it is a reasonable approximation to neglect material strength and treat the reactants as a fluid. The material properties of both the reactants and the products are characterized by an EOS. Partly burned HE is assumed to be described by a mixture EOS, $P(V, e, \lambda)$, which interpolates between the reactants ($\lambda = 0$) and the products ($\lambda = 1$) equations of state.

The Forest fire model is based on three further assumptions; pressure-temperature equilibrium for partly burned HE, single-curve buildup principle, and a pressure dependent fitting form for the burn rate. We discuss each

[2]There is an extension of the Forest fire model for build-up of a detonation wave, see [Mader, 1998, App. A.10]. This mimics a second reaction by interpolating between two products EOS.

of these assumptions in turn.

2.1 Pressure-temperature equilibrium

A mixture EOS requires a closure assumption. If burn is volumetric in nature, reactants and products would be well mixed. Then it is reasonable to treat partly burned HE in pressure-temperature equilibrium.

Let subscript '1' denote the reactants and subscript '2' denote the products. Thus, the mass fraction of the reactants is $\lambda_1 = 1 - \lambda$, and the mass fraction of the products is $\lambda_2 = \lambda$. The pressure-temperature equilibrium equation of state, $P(V, e, \lambda)$, is determined by the equations

$$\begin{aligned} V &= \lambda_1 V_1 + \lambda_2 V_2 \ , \\ e &= \lambda_1 e_1 + \lambda_2 e_2 \ , \\ P &= P_1(V_1, e_1) = P_2(V_2, e_2) \ , \\ T &= T_1(V_1, e_1) = T_2(V_2, e_2) \ . \end{aligned} \tag{3}$$

If the component EOS are thermodynamically consistent,[3] then it can be shown that Eq. (3) has a unique solution, provided that the domain of the components include the (P, T) regime of interest. Moreover, the mixture EOS is thermodynamically consistent; see for example [Menikoff, 2007]. Hence, the mixture sound speed is well defined, and Eq. (1) maintains the usual hyperbolic properties of the Euler equations.

Numerically, a pressure-temperature equilibrium EOS is computed with an iterative algorithm to solve Eq. (3). Many algorithms restrict the component EOS such that the specific heat, $C_V = \partial_T e|_V$, is constant and the Grüneisen coefficient, $\Gamma = V\partial_e P|_V$, is a function of only V. Due care is needed to ensure that each iteration is within the domain of the component EOS and that the iterations converge. Because of the reactive source terms, simulations are much more sensitive to numerical errors in evaluating the mixture EOS for an explosive than for inert materials.

Based on the physical processes that take place at the mesoscale, other closure assumptions are possible. Reaction in a heterogeneous explosive is due to hot spots or localized regions of high temperature. Suppose a hot spot reacts on a short temporal scale and gives rise to a deflagration front. This

[3] P and T derivable from a thermodynamic potential (such as the Helmholtz free energy), the specific heat $C_V = \partial_T e|_V > 0$, and the isothermal sound speed squared $c_T^2 = -V^2 \partial_V P|_T > 0$.

is the underlying physical picture behind the ignition and growth model of Lee and Tarver [1980]. Across the front, the reactants and products are in neither pressure nor temperature equilibrium. Typically, the pressure jump across a deflagration front is small. However, at the Chapman-Jouguet (CJ) pressure the deflagration speed can be a significant fraction of the detonation speed [Esposito et al., 2003]. Since $\Delta P/\Delta V = -(\rho D)^2$, the pressure jump across a deflagration front may not be negligible.

A non-equilibrium treatment would require a two-phase fluid model in order to track the specific energy and specific volume separately for the reactants and products. One possibility for a mixture rule is to track the shock pressure and replace temperature equilibrium condition with the condition that the reactants are on the isentrope of the shock state; see [Johnson et al., 1985]. Another mixture rule assumes that the pressure is a weighted average of the component pressures;

$$P(V, e) = \lambda_1 P_1(V, e) + \lambda_2 P_2(V, e) \ .$$

Simple ad hoc closure assumptions run the risk of a thermodynamic inconsistent mixture EOS and unphysical behavior for solutions to the reactive Euler equations.

2.2 Single-curve buildup principle

Shock ignition of heterogeneous explosives have been studied by measuring the x–t trajectory of the lead front; see Campbell et al. [1961a]. The transition to a detonation wave is very abrupt. Consequently, trajectories for different initiation pressures can be compared by shifting the (x, t) origin to correspond to the transition point[4]. It is then observed that the measured trajectories lie on top of each other. This led to the hypothesis that the x–t trajectory for a shock-to-detonation transition is independent of the starting pressure; see [Mader, 1965, App. D, p. 119]. The hypothesis is known as the *single-curve buildup principle*.

The most careful test of the principle has been performed on an RDX based PBX by Linstrom [1966]. Within the uncertainties in the measurements, Lindstrom found that a single trajectory is consistent with the RDX

[4]The transition point is somewhat fuzzy as it can not be defined more accurately than the reaction zone width for a steady detonation wave. Typically, this uncertainty is small compared to the spatial interval over which a trajectory is measured.

data. Another study by Dick [1981] found reasonable but not perfect agreement among front trajectories for PBX 9404 and PBX 9502. However, Dick used unpublished data of other researchers and did not propagate uncertainties in the data through his analysis. Later, in subsection 5.2 analyzing the effect of flow gradients, we infer that the single-curve buildup principle implies the reaction rate at the front dominates the shock acceleration. This is compatible with the concept that the shock front activates hot spots which determine the effective burn rate.

An important consequence of the single-curve buildup principle is that shock ignition can be characterized by the run-to-detonation distance as a function of ignition pressure. Run distance versus pressure, on a log-log scale, is known as a *Pop plot*[5]. This is discussed in more detail in sec. 4.

2.2.1 Reactive Hugoniot

The same experiments that are used to determine the Pop plot also measure points on the Hugoniot locus. Early experiments on PBX 9404 indicated that in the (u_p, u_s)–plane, the locus is a straight line starting at $(0, c_0)$ and extrapolating near the CJ state; see [Ramsay and Popolato, 1965, fig. 2]. This led to the further hypothesis that the lead front in a shock-to-detonation transition is a reactive shock; see [Ramsay and Popolato, 1965] and [Mader, 1970]. Other Hugoniot data for PBX 9404 [Gibbs and Popolato, 1980, pp. 359–362] do not extrapolate to the CJ state. Nevertheless, the derivation of the Forest fire model utilizes the reactive shock hypothesis.

The ambiguity of whether or not the lead front is a reactive shock, occurs because of the difficulty in measuring the shock state for an HE. The shock state is inferred from a measurement of the shock velocity. Typically, the shock velocity is determined by the transit time for a given distance of run. If the transit time is not sufficiently small then the reaction over the measurement interval may be significant. Thus, limited spatial and temporal resolution can result in a systematic error corresponding to a reactive shock.

2.3 Pressure dependent rate

The essence of the Forest fire model is an analysis that determines the reaction rate at the shock front necessary for the shock trajectory to agree with

[5]Named after its originator Alphonse Popolato.

the trajectory derived from Pop-plot data and the single-curve buildup principle. An assumption is needed on the spatial gradients behind the shock front. The original model used the assumption that $\partial_x P = 0$. Later, in subsection 5.2 we show how to account for the flow gradients. Moreover, the needed information about the flow gradients can be obtained from velocity gauge data.

Extending the rate to a general state requires a further assumption on the fitting form used for the rate. The choice for the Forest fire model is to take the rate to be the product of a particular function of λ (namely, $1-\lambda$) and a function of pressure, $\mathcal{R}_{\rm FF}(P)$; *i.e.*, Eq. (2). The rate at the shock front is used to fit $\mathcal{R}_{\rm FF}(P)$. Later we argue that varying the 'reaction order' (*i.e.*, replacing $1-\lambda$ with $(1-\lambda)^n$) could enable the model to fit additional detonation wave properties; such as velocity gauges or the curvature effect.

The reactive shock locus can be parameterized by a single thermodynamic variable. The choice of pressure to parameterize the shock locus and hence the reactive rate, enables the model to be well behaved in numerical simulations. Acoustic waves provide a feedback mechanism that corrects local numerical errors in the pressure. In contrast, numerical errors in entropy are persistent, and affect both the density and temperature.

Plastic-bonded explosives have a small amount of porosity. The ignition sensitivity of a PBX increases with porosity. One mechanism for generating hot spots is based on pore collapse; see for example [Mader, 1965] and [Menikoff, 2004]. Therefore, it is plausible that shock pressure is the driving force that activates hot spots. Consequently it is reasonable that the effective reaction rate would be dominated by pressure.

3 Reactive Hugoniot locus

A partly burned Hugoniot locus, with fixed burn fraction λ, is defined by the Hugoniot equation

$$e = e_0 + \tfrac{1}{2}(P + P_0)(V_0 - V) \ , \tag{4}$$

where $P = P(V, e, \lambda)$. As λ increases these loci interpolate from the reactants Hugoniot locus ($\lambda = 0$) to the products detonation locus ($\lambda = 1$). The mixture EOS is assumed to satisfy the condition that the pressure increases with burn fraction; $\partial_\lambda P > 0$. It can then be shown that the loci in the (V, P)–plane with different values of λ do not cross.

A reactive Hugoniot locus can be specified by a u_s–u_p relation for the shock velocity as a function of particle velocity; $u_s(u)$. For a given u, the Hugoniot jump conditions determine a point in the (V, P)–plane; namely, $V = (1 - u/u_s)V_0$ and $P = P_0 + \rho_0\, u\, u_s$. This point lies on a unique partly burnt locus. Hence, the value of λ is determined.

The partly burned Hugoniot loci have a subsonic (strong) branch and a supersonic (weak) branch. The two branches meet at a sonic point, which we refer to as the CJ state for a partly burned locus. We require a partly burned reactive shock to be on the subsonic branch; *i.e.*, $u + c > u_s$. The frozen sound speed, c, is determined from the EOS by

$$(\rho\, c)^2 = -\partial_V P + P\partial_e P \ ,$$

where the partial derivatives are at fixed λ.

The value of λ on the reactive Hugoniot locus can also be found from an ODE. It is convenient to parameterize the reactive locus by u. In terms of the mixture EOS, the shock pressure can be expressed as

$$P_s(u) = P\Big(V(u), e(u), \lambda(u)\Big) \ .$$

Then by applying the chain rule to the derivative of the shock pressure with respect to u, one obtains

$$\frac{\mathsf{d}\lambda}{\mathsf{d}u} = \frac{\frac{\mathsf{d}P}{\mathsf{d}u} - (\partial_V P)\frac{\mathsf{d}V}{\mathsf{d}u} - (\partial_e P)\frac{\mathsf{d}e}{\mathsf{d}u}}{\partial_\lambda P} \ , \tag{5}$$

where the partial derivatives are based on the mixture EOS (see App. A), and $\frac{\mathsf{d}}{\mathsf{d}u}$ is the derivative along the Hugoniot locus.

From the shock jump relations

$$V(u) = \left[1 - \frac{u}{u_s}\right] V_0 \ , \tag{6a}$$

$$e(u) = e_0 + P_0\, V_0 \left[\frac{u}{u_s}\right] + 0.5\, u^2 \ , \tag{6b}$$

$$P(u) = P_0 + \rho_0\, u\, u_s \ , \tag{6c}$$

we obtain

$$\frac{\mathsf{d}V}{\mathsf{d}u} = -\left[1 - \frac{u}{u_s}\frac{\mathsf{d}u_s}{\mathsf{d}u}\right]\frac{V_0}{u_s} \ , \tag{7a}$$

$$\frac{\mathsf{d}e}{\mathsf{d}u} = u + \left[1 - \frac{u}{u_s}\frac{\mathsf{d}u_s}{\mathsf{d}u}\right]\frac{P_0\,V_0}{u_s} \ , \tag{7b}$$

$$\frac{\mathsf{d}P}{\mathsf{d}u} = \left[1 + \frac{u}{u_s}\frac{\mathsf{d}u_s}{\mathsf{d}u}\right]\rho_0 u_s \ . \tag{7c}$$

The ODE, Eq. (5), is closed by specifying a u_s–u_p relation for the reactive Hugoniot locus. Typically, it is assumed that $u_s(u)$ is a linear function; $u_s = c_0 + s\,u$. In the limiting case in which the reactive locus goes through the CJ state, $\frac{\mathsf{d}u_s}{\mathsf{d}u} = s = (D_{\mathrm{CJ}} - c_0)/u_{\mathrm{CJ}}$, where D_{CJ} is the detonation speed and u_{CJ} is the particle velocity at the CJ state.

We note that for a single point on the reactive locus, $\lambda(u)$ can be found by solving the non-linear equation

$$P(u) = P(V(u), e(u), \lambda) \ ,$$

where $V(u)$, $e(u)$ and $P(u)$ are determined from the shock jump relations, Eq. (6), and $P(V, e, \lambda)$ from the mixture EOS. Integrating the ODE is more efficient for evaluating the entire locus; *i.e.*, over the interval $0 \le \lambda(u) \le 1$.

3.1 Example — PBX 9501

Example reactive and partly burned Hugoniot loci are shown in fig. 1. The loci are calculated from an EOS for PBX 9501. The reactants EOS is based on Birch-Murnaghan form for the cold curve fit to HMX isothermal compression data [Menikoff and Sewell, 2004] with the initial density and sound speed adjusted to match PBX 9501. Analogous to the Debye model, C_V is taken to be a function of a scaled temperature, $T/\theta(V)$, where the Grüneisen coefficient is given by $\Gamma(V) = -\mathsf{d}\ln(\theta)/\mathsf{d}\ln(V)$. At the initial density, the temperature dependence of C_V is fit to molecular dynamics calculations of Goddard et al. [1998, fig. 4.13]. A tabular Sesame EOS is used for the products. The table generated by Shaw [2004] is based on PBX 9501 overdriven detonation wave data [Fritz et al., 1996] and release wave data [Hixson et al., 2000] for high pressures ($P > 20\,\mathrm{GPa}$), and cylinder experiment data at lower pressures. In addition, the reactive Hugoniot locus is based on a linear u_s–u_p relation connecting the initial state to the CJ state.

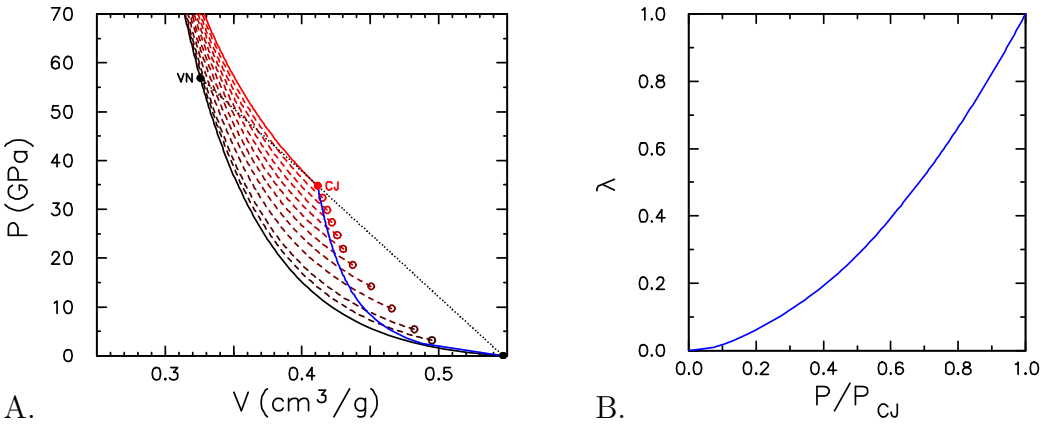

Figure 1: Hugoniot loci for PBX 9501. A. Partly burned and reactive Hugoniot loci in (V, P)–plane. Black curve is reactant locus ($\lambda = 0$) and red curve is product locus ($\lambda = 1$). CJ states are indicated by open circles. Blue curve is reactive locus based on linear u_s–u_p relation for the case going through the CJ state. Dotted black line is Rayleigh line through CJ state. B. Reaction progress variable as function of pressure along reactive locus.

4 Run to detonation

A shock-to-detonation transition is characterized, to a large extent, by the x–t trajectory of the lead front. Shock initiation trajectories for many explosives have been measured with wedge experiments; see [Campbell et al., 1961a] and [Gibbs and Popolato, 1980, part II, sec. 4.1]. Comparison of the trajectories for different initiation pressures led to the single-curve buildup principle. A consequence of this principle is that shock initiation can be characterized by a Pop plot or run-to-detonation distance as a function of initiation pressure. The wedge experiments, which are the basis for the Pop plot, are described next.

4.1 Wedge experiment

For solid explosives, it is difficult to measure hydrodynamics quantities in the interior. The surface, however, is readily accessible to measurement. The wedge experiment is a clever design for measuring the trajectory of the lead front for a shock-to-detonation transition. The experimental configuration is shown in fig. 2. A planar shock wave from an explosive drive system is used

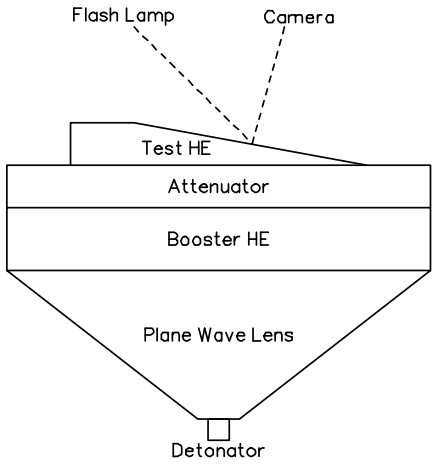

Figure 2: Schematic of wedge experiment.

to initiate a wedge shaped test sample of HE. The pressure of the initiation shock can be varied by adjusting the thickness of the attenuator and the selection of attenuator material or booster explosive.

Breakout of the reactive shock on the wedge surface changes its reflectivity. First motion of points along the wedge are recorded with a streak camera. Breakout of the shock also gives rise to a reflected rarefaction. However, because of the small wedge angle, the rarefaction does not influence the reactive front within the test HE. Hence the measured trajectory corresponds to the motion of a planar wave, *i.e.*, one-dimensional flow.

A typical x–t trajectory for a shock initiated detonation is shown in fig. 3. The transition to detonation is seen to be very abrupt. A less subjective and more accurate determination of the transition point can be made using a global fitting form for the trajectory data; see [Gustavsen et al., 1999] and [Hill and Gustavsen, 2002].

The data shown in fig. 3 is actually from an experiment that provides trajectory data equivalent to a wedge experiment but using a newer technique [Gustavsen et al., 1999]. Rather than an explosive drive system, the initiating shock is generated by the impact of a projectile launched by a gas gun. A magnetic tracker gauge is used to determine the front trajectory. In addition, magnetic velocity gauges measure Lagrangian time histories at a number of positions. Thus one experiment can provide data on the evolution of the velocity profile (see fig. 9) during a shock-to-detonation transition, as well as

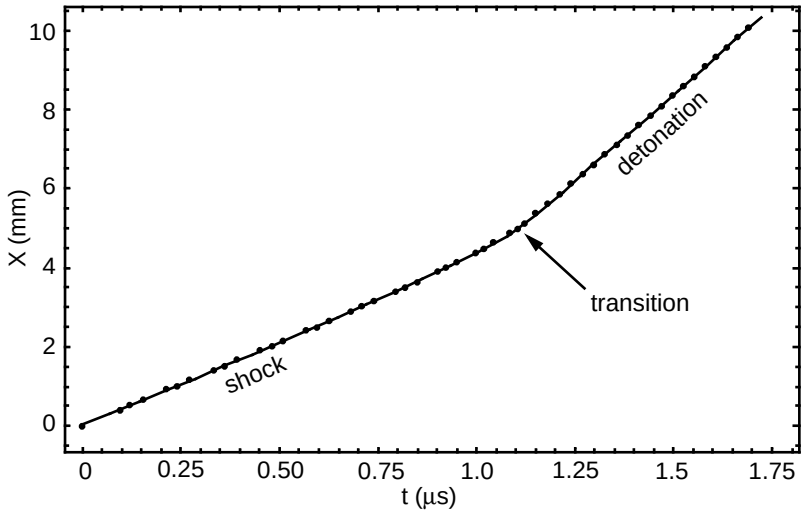

Figure 3: Front trajectory for shock-to-detonation transition in PBX 9501. Data points (dots) and fit (curve) are from Gustavsen et al. [1999, fig. 11]; reproduced with permission of the authors. Velocity gauge data for the same experiment is shown in fig. 9.

the front trajectory.

4.1.1 Initiation pressure

In addition to the front trajectory, one needs to know the initiation or drive pressure. This is determined as follows. Timing pins or other gauges are used to measure the free surface velocity of the attenuator. In conjunction with the EOS of the attenuator, the free surface velocity determines the incident shock strength in the attenuator. The initial slope of the x–t trajectory determines the initial shock velocity in the test HE. The intersection of the Rayleigh line with slope $\rho_{\mathrm{HE}} u_s$ and the reflected shock locus in the attenuator determines the initiation pressure for the test HE. The graphical construction is illustrated in fig. 4.

The impedance match for the drive pressure also determines a point on the Hugoniot locus of the test explosive. A leading source of uncertainty is the measurement of the initial shock velocity. The determination of the initial slope of the shock trajectory requires fitting data over an interval about the wedge tip. To facilitate construction the wedge tip may be truncated, thus

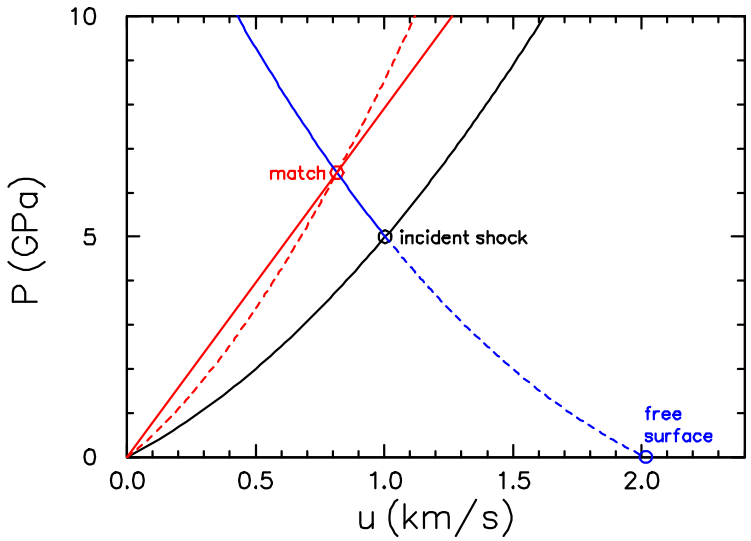

Figure 4: Example of graphical solution to impedance match for PMMA attenuator and PBX 9501 test HE. Black curve is incident Hugoniot locus for attenuator. Blue curve is reflected wave locus in attenuator; solid line is shock and dashed line is rarefaction. Solid red curve is Rayleigh line with slope $\rho_{\mathrm{HE}} u_s$. Dashed red curve is Hugoniot locus for the HE. The free surface velocity and incident shock in the attenuator are labeled. The match point corresponds to the initiation pressure for test HE in the wedge experiment.

blunting the sharp wedge angle. Consequently the initial shock velocity may actually correspond to the value after a small distance of run during which some reaction occurs. In addition, the shock velocity is approximated by either a finite difference form ($\Delta x/\Delta t$) or the derivative of a running average of $x(t)$. Hence the shock velocity is an average over a non-zero interval. The extent of the trajectory used to determine the initial shock velocity is a resolution issue that affects whether the Hugoniot locus is interpreted as reacted or unreacted.

Alternate techniques are now available to measure the unreacted shock Hugoniot [Sheffield et al., 2004]. These involve measuring time histories of the velocity at the HE interface. With a resolution of a few ns, one can distinguish the initial shock velocity from the subsequent change due to reaction. Also available are techniques for isentropic compression to high pressure. In a PBX, isentropic compression generates fewer and weaker hot

spots than shock compression. Thus, the reactants EOS can be based on isentropic compression data rather than Hugoniot data; see [Hooks et al., 2006, Baer et al., 2006].

4.2 Pop plot

Distance-of-run to detonation can be fit to a straight line on a log-log plot [Ramsay and Popolato, 1965];

$$\log_{10}\Big[(P - P_\star)/P_{\text{ref}}\Big] = a - b \times \log_{10}[x/x_{\text{ref}}] \tag{8}$$

where $P_\star$ represents a pressure threshold. This is known as a *Pop plot*. The reference dimensions P_{ref} and x_{ref} correspond to the choice of units for pressure and length, respectively. The threshold pressure was added by Linstrom [1966] to achieve a better fit at low pressures to data on a RDX based PBX. Typically, wedge data does not extend to low pressures and the Pop plot is fit with $P_\star = 0$.

Wedge data for many explosives can be found in Gibbs and Popolato [1980, part II, sec. 4.1]. In addition, they give Pop plot parameters with units of $P_{\text{ref}} = 1\,\text{GPa}$ and $x_{\text{ref}} = 1\,\text{mm}$. Example Pop plots are shown in fig. 5 for three explosives. PBX 9501 and PBX 9404 are both HMX based explosives. Their Pop plots show that the formulation of a PBX (binder and grain distribution) can affect the sensitivity, especially at low pressures. PBX 9502 is an insensitive explosive based on TATB. For a given pressure, it has larger distance of run than the more sensitive HMX based PBXs. Since the Pop plot curves can cross, the sensitivity of different explosives do not necessarily have a strict ordering.

We note that data points from wedge experiments are usually limited to distances of run in the range of 1 to 20 mm. Difficulties occur for small run distances (high drive pressures) due to the accuracy at which the transition to detonation point on the x–t trajectory can be determined, and for large run distances (low drive pressures) due to rarefaction from the side of the wedge or pressure gradient in the drive system. With careful design and a large test sample, distance of run measurements can be extended up to 40 or 50 mm. Sensitive explosives require thick attenuators in the drive system and have a fairly uniform drive pressure. Measurements for insensitive explosives require thin attenuators and may be affected by pressure gradient from Taylor wave in the booster explosive.

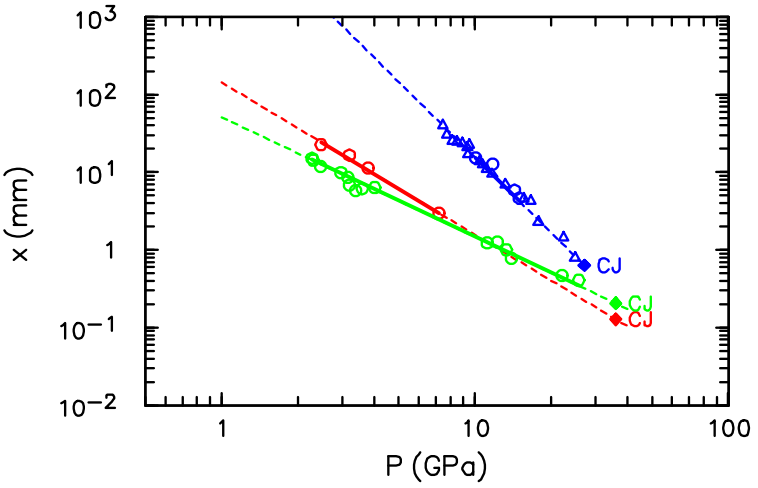

Figure 5: Example of Pop plots for three explosives. Red, green and blue lines are for PBX 9501, PBX 9404 and PBX 9502, respectively. Solid lines correspond to domain of fit to experimental data, and dashed lines are extrapolation. Solid diamonds are at CJ pressure of each explosive and circles denote data points. Fitting parameters and data points are from Gibbs and Popolato [1980]: PBX 9501, p. 115 and table 4.17; PBX 9404, p. 93 and table 4.18; PBX 9502, p. 126 and table 4.31. In addition, for PBX 9502, triangles are data points from [Dick et al., 1988, table I].

For the reactive shock model, in principle, distance-of-run to detonation goes to zero at the CJ pressure, *i.e.*, $x \to 0$ as $P \to P_{\mathrm{CJ}}$. It is noteworthy that the experimental Pop plot extrapolated to CJ pressure gives a value for the distance of run comparable to the reaction zone width. For example, on the PBX 9501 Pop plot, the distance of run at the CJ pressure is 0.13 mm, while the experimental value for the reaction zone width is about 0.025 mm at $\lambda = 0.90$; see [Menikoff, 2006] and [Gustavsen et al., 1998a,b]. The reaction zone width introduces a length scale. It can be used to shift the origin of the x–t trajectory. This helps to regularize the rate $\mathcal{R}(P)$ at P_{CJ} constructed in the next section.

Similarly, the time-to-detonation can be fit with a straight line on log-log plot. In principle, distance-to-detonation and time-to-detonation determine $u_s(P)$ for a reactive shock. But the inaccuracy due to uncertainties in the measurements is severe. As an example, for PBX 9501 [Gibbs and Popolato,

1980, p. 115]

$$\log(P) = (1.10 \pm 0.04) - (0.51 \pm 0.03)\log(x) \ ,$$
$$\log(P) = (0.76 \pm 0.01) - (0.45 \pm 0.03)\log(t) \ .$$

It follows that $u_s = \frac{\mathsf{d}x}{\mathsf{d}t} = \frac{\mathsf{d}P/\mathsf{d}t}{\mathsf{d}P/\mathsf{d}x}$ can be expressed in terms of P as

$$u_s \propto P^{\left[\frac{1}{0.45\pm0.03} - \frac{1}{0.51\pm0.03}\right]} \propto P^{0.26\pm0.26} \ .$$

Clearly the uncertainty is too large for this expression to be useful.

Alternatively, the shock velocity can be determined from the x–t trajectory, and then using the single-curve buildup principle associated with the shock pressure at the corresponding distance of run. In other words, $u_s(P)$ can be determined from the shock trajectory and the Pop plot. The shock relation, $P = P_0 + \rho_0 u_p u_s$, would then determine a self-consistent u_s–u_p relation for the Hugoniot locus of the reactive shock.

To illustrative these relations, we use the Hugoniot locus in fig. 1 and the Pop plot in fig. 5 to calculate the x–t trajectory for PBX 9501. For a linear u_s–u_p relation, the shock velocity in terms of the pressure is given by

$$u_s(P) = \tfrac{1}{2}\left(c_0 + \left[c_0^2 + 4s\,(P - P_0)\,V_0\right]^{1/2}\right) \ .$$

From Eq. (8) for the Pop plot, $P(x) = \frac{10^a}{x^b}$. Hence $u_s(P(x))$ determines the shock velocity as a function of distance. The corresponding time on the shock trajectory is

$$t(x) = t_{\rm CJ} + \int_0^x \frac{\mathsf{d}x}{u_s(x)} \ ,$$

where relative to the Pop plot x is replaced by $-x$ in order that the detonation transition occurs at $x = 0$ and $t = t_{\rm CJ}$. It is natural to take $t_{\rm CJ} = x_{\rm CJ}/D_{\rm CJ}$ where $x_{\rm CJ}$ is the distance of run on the Pop plot at the CJ pressure. The result, shown in fig. 6, is comparable to the measured trajectory in fig. 3. Also shown in fig. 6 is the reaction progress variable. The abrupt transition to detonation is due to the rapid change in λ as the reaction rate increases with shock pressure. This is the analog of an induction time for a homogeneous explosive with an Arrhenius rate.

The corresponding shock velocity and time-to-detonation for the model are shown in fig. 7. As with the standard Pop plot, time-to-detonation is

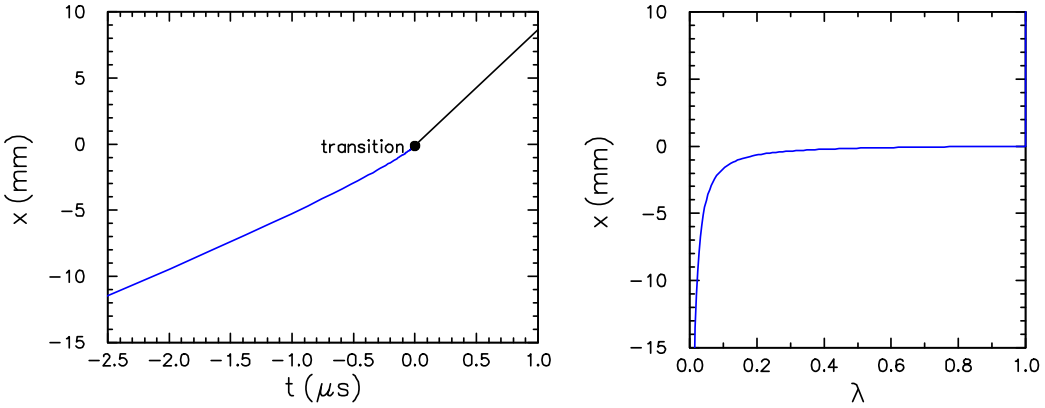

Figure 6: Shock trajectory for PBX 9501 computed from Hugoniot locus in fig. 1 and Pop plot in fig. 5.

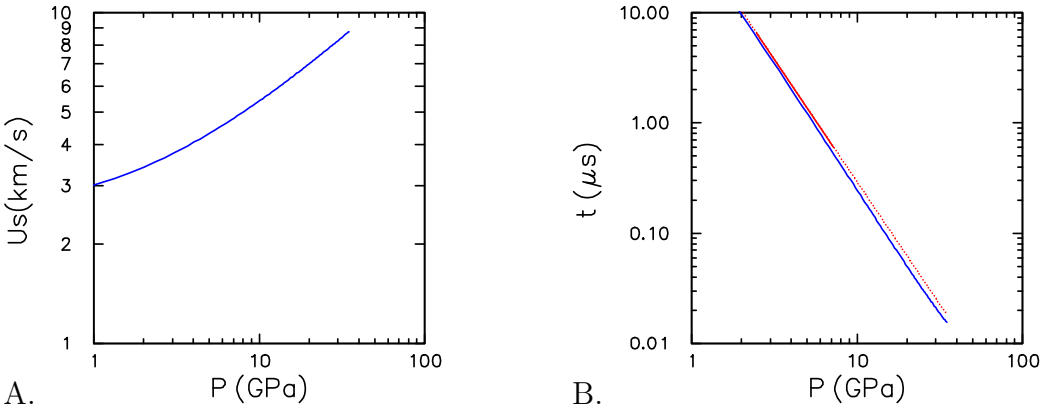

A. B.

Figure 7: A. Shock velocity versus pressure on reactive Hugoniot locus shown in fig. 1. B. Blue curve is time-to-detonation corresponding to trajectory in fig. 6. Red curves are based on fit parameters from Gibbs and Popolato [1980, p. 115]; solid corresponds to range of data and dotted to extrapolation.

nearly linear on a log-log scale. However, as discussed above, linear relations for both distance-to-detonation and time-to-detonation are not consistent with the shock velocity. Nevertheless, it can be seen that to a good approximation both variables may be treated as linear.

5 Reaction rate analysis

The PDEs for reactive flow, Eq. (1), can be written in characteristic form; see App. B. The characteristic equations have source terms from the reaction rate. For the forward characteristic, Eq. (26a),

$$[\partial_t + (u+c)\partial_x]P + \rho c\,[\partial_t + (u+c)\partial_x]u = (\partial_\lambda P)\mathcal{R} \ ,$$

where ∂_λ is at fixed V and e. To apply this equation at the shock front, we decompose the characteristic derivative as

$$[\partial_t + (u+c)\partial_x] = [\partial_t + u_s\partial_x] + (u+c-u_s)\partial_x \ ,$$

and note that $\frac{\mathsf{d}}{\mathsf{d}t_s} = [\partial_t + u_s\partial_x]$ is the derivative along the shock front. Then the characteristic equation can be re-expressed as

$$\frac{\mathsf{d}P}{\mathsf{d}t_s} + \rho c\,\frac{\mathsf{d}u}{\mathsf{d}t_s} = (\partial_\lambda P)\mathcal{R} - \Big(u+c-u_s\Big)\Big(\partial_x P + \rho c\,\partial_x u\Big) \ . \tag{9}$$

The Forest fire model requires an additional assumption on the flow gradients behind the front.

The gradient terms and the shock growth terms are partly related by the shock change equations, App. C. To separate out the effects, we re-express Eq. (9) in terms of two independent derivatives; $\frac{\mathsf{d}P}{\mathsf{d}t_s}$ and $\frac{\mathsf{d}u}{\mathsf{d}t}$, where $\frac{\mathsf{d}}{\mathsf{d}t} = \partial_t + u\partial_x$ is the convective time derivative. First, the momentum equation in Lagrangian form, Eq. (21b), can be used to eliminate the pressure gradient; $\partial_x P = -\rho\frac{\mathsf{d}u}{\mathsf{d}t}$. Second, the velocity gradient can be expressed in terms of time derivatives as

$$\partial_x u = \Big(\frac{\mathsf{d}u}{\mathsf{d}t_s} - \frac{\mathsf{d}u}{\mathsf{d}t}\Big)/(u_s - u) \ .$$

After some algebra, Eq. (9) can be re-expressed as

$$(\partial_\lambda P)\mathcal{R} = \frac{\mathsf{d}P}{\mathsf{d}t_s} + \rho(u_s-u)\Big[z^2\frac{\mathsf{d}u}{\mathsf{d}t_s} - (z^2-1)\frac{\mathsf{d}u}{\mathsf{d}t}\Big] \ , \tag{10}$$

where $z = c/(u_s-u)$. We note that $z \geq 1$, since the flow behind the shock front is subsonic. Moreover, $z = 1$, when the flow behind the shock is sonic; *e.g.*, at the CJ state.

Next we can use the chain rule to replace

$$\frac{\mathsf{d}u}{\mathsf{d}t_s} = \frac{\mathsf{d}P}{\mathsf{d}t_s}\Big/\Big(\frac{\mathsf{d}P}{\mathsf{d}u}\Big)_h \ ,$$

where the derivative along the Hugoniot locus, $(\mathsf{d}P/\mathsf{d}u)_h$, is given in terms of the u_s–u_p relation for the reactive Hugoniot by Eq. (7c). Substituting this relation plus the momentum jump condition, $\rho(u_s - u) = \rho_0 u_s$, into Eq. (10) yields

$$(\partial_\lambda P)\mathcal{R} = \left[1 + \frac{\rho_0\, u_s\, z^2}{\left(\frac{\mathsf{d}P}{\mathsf{d}u}\right)_h}\right] \frac{\mathsf{d}P}{\mathsf{d}t_s} - \rho_0\, u_s \big(z^2 - 1\big) \frac{\mathsf{d}u}{\mathsf{d}t} \ .$$

The time derivative of the shock pressure can be expressed as a spatial derivative of the shock trajectory $\frac{\mathsf{d}P}{\mathsf{d}t_s} = u_s \frac{\mathsf{d}P_s}{\mathsf{d}x}$. This can be determined from Popplot data. The Lagrangian time derivative of the velocity, $\frac{\mathsf{d}u}{\mathsf{d}t}$, can be determined from velocity gauge data.

The original derivation of the Forest fire model by Mader and Forest [1976] assumed that the pressure gradient at the front is zero. A zero pressure gradient is equivalent to $\frac{\mathsf{d}u}{\mathsf{d}t} = 0$. After substituting Eq. (7c) for the Hugoniot derivative, the rate at the shock front with the zero pressure gradient assumption can be expressed as

$$\mathcal{R}_0 = (\partial_\lambda P)^{-1} \left[1 + \frac{\rho_0\, u_s\, z^2}{1 + \frac{u}{u_s}\frac{\mathsf{d}u_s}{\mathsf{d}u}}\right] u_s \frac{\mathsf{d}P_s}{\mathsf{d}x} \ . \tag{11}$$

Alternatively, the same rate can be determined from the shock change equations; see App. C.

More generally, including the pressure gradient, the rate at the front can be expressed as

$$\mathcal{R} = (1 - g)\, \mathcal{R}_0 \ , \tag{12}$$

where

$$g = \Big[z^2 - 1\Big] \left[\frac{1 + \frac{u}{u_s}\frac{\mathsf{d}u_s}{\mathsf{d}u}}{1 + \frac{u}{u_s}\frac{\mathsf{d}u_s}{\mathsf{d}u} + z^2}\right] \left[\frac{\frac{\mathsf{d}u}{\mathsf{d}t}}{V_0 \frac{\mathsf{d}P_s}{\mathsf{d}x}}\right] \ . \tag{13}$$

Typically, the third factor is positive and less than 2. In this case, the original Forest fire assumption leads to an upper bound on the rate; *i.e.*, $\mathcal{R} \leq \mathcal{R}_0$. Moreover, the first factor can be written as $z^2 - 1 = (z+1)(c+u-u_s)/(u_s-u)$, and the factor $c+u-u_s$ suppresses the effect of the pressure gradient because the flow behind the reactive shock front is near sonic. This is quantitified in a following subsection.

Up to this point, the analysis for the rate at the front is general. It can be applied to any burn model, even with the reactive Hugoniot locus replaced

by the unburnt or reactant Hugoniot locus. That is to say, equations (11)–(13) determine the rate at the shock front needed to fit shock-to-detonation transition data. This provides a constraint that can be used when calibrating rate parameters.

5.1 Forest fire rate

Utilizing Eq. (8) for the Pop plot (with x replaced by $-x$),

$$\frac{\mathsf{d}P_s}{\mathsf{d}x} = b\,\frac{P - P_\star}{x} = b\,10^{-a/b}\,[(P - P_\star)/P_{\rm ref}]^{1+1/b}\,\frac{P_{\rm ref}}{x_{\rm ref}}\ . \tag{14}$$

Moreover, the reactive Hugoniot can be parameterized by the pressure. Hence, at the front, $\mathcal{R}$ can be parameterized by the shock pressure. The Forest fire model assumes that there is a global rate of the form, Eq. (2),

$$\mathcal{R}(P,\lambda) = (1-\lambda)\mathcal{R}_{\rm FF}(P)\ ,$$

and fits the function $\mathcal{R}_{\rm FF}$ to the rate at the front with λ from the reactive shock Hugoniot; *i.e.*, $\mathcal{R}_{\rm FF}(P) = \mathcal{R}_{\rm front}(P)/[1-\lambda_s(P)]$. Moreover, the original formulation, that neglects the pressure gradient, uses $\mathcal{R}_0$, Eq. (11), for the rate at the front. In the next subsection we show that g is small, and hence $\mathcal{R}_0$ is the dominant factor in the rate.

We note that the rate $\mathcal{R}_0$ is proportional to $\mathsf{d}P_s/\mathsf{d}x$ and that the pressure derivative, Eq. (14), does not vanish at the CJ pressure. Two limiting cases, which dependent on whether or not the reactive Hugoniot ends at the CJ state, are instructive. First, suppose that the reactive Hugoniot does end at the CJ state. Then $\mathcal{R}_{\rm FF}(P)$ would have a singularity at $P = P_{\rm CJ}$ since $\lambda = 1$. The singularity is due in part to extrapolating the Pop plot and the fact that a first order rate gives rise to an exponential tail. In contrast, a rate proportional to $(1-\lambda)^n$ with $n < 1$ would lead to a finite reaction zone. The singularity could then be removed in a consistent manner by modifying the Pop plot. For example, one can take a transition distance x_1 such that the pressure on Pop plot corresponds to point on reactive shock locus with $\lambda = 0.95$, and then redefine distance of run for $x < x_1$ by

$$x = x_{\rm CJ} + A(P_{\rm CJ} - P)^{1-n}\ ,$$

where the parameters A and $x_{\rm CJ}$ are chosen such that $P(x)$ and $\mathsf{d}P/\mathsf{d}x$ are continuous at $x = x_1$. By construction, both $\mathsf{d}P/\mathsf{d}x$ and $(1-\lambda)$ would go to zero at the CJ state and $\mathcal{R}_{\rm FF}(P_{\rm CJ})$ would be finite.

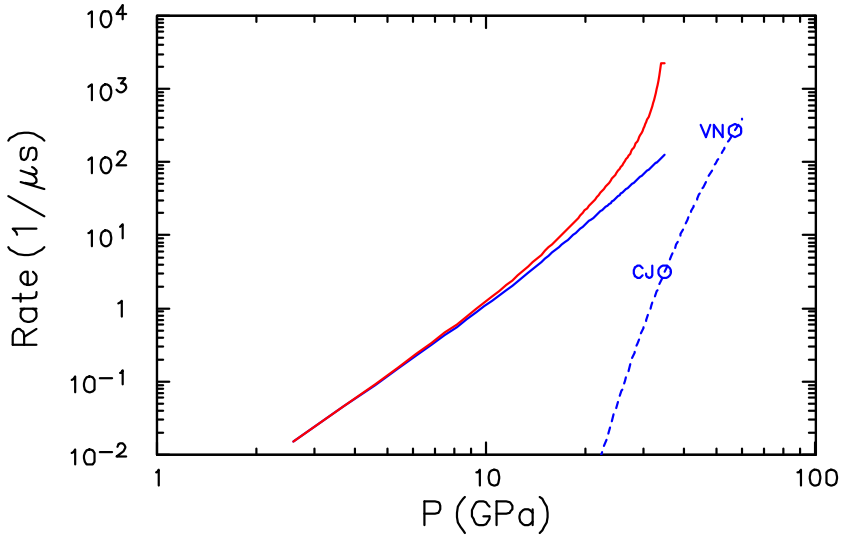

Figure 8: Forest fire rate for PBX 9501 using for distance of run-to-detonation $\log_{10}(P/\text{GPa}) = 1.10 - 0.51\log_{10}(x/\text{mm})$ from Gibbs and Popolato [1980, p. 115]. Solid blue curve is the total reaction rate, $\mathcal{R}_0$, and red curve is pressure dependent rate factor, $\mathcal{R}_{\text{FF}}$, with λ cutoff at 0.95 to avoid singularity. Dashed blue line is chemical rate based on reactant shock temperature and Arrhenius rate compatible with measured reaction zone profile for steady planar detonation wave. Circles denote bulk rate at shock pressure corresponding to the CJ and VN states.

Alternatively, suppose in the (u_p, u_s)–plane the reactive Hugoniot passes to the left of the CJ state and ends on the Rayleigh line through the CJ state with $\lambda < 1$. Then Eqs. (11) and (14) would give finite values for $\mathcal{R}_{\text{FF}}(P)$ up to a pressure slightly larger than P_{CJ}. The steady reaction zone profile, discussed in sec. 6.2.1, would have the form shown in fig. 11 in which the lead shock pressure exceeds the CJ pressure but is less than the VN spike pressure. This is compatible with the experimental observation for initiation experiments that the shock velocity does not overshoot the detonation speed. Both of these prescriptions regularize the rate near P_{CJ} by using an *ad hoc* extrapolation of data and neglect the asymptotic appoach to steady state. There is no physical reason to prefer one regularization over the other.

As an example, the Forest fire rate for PBX 9501 is shown in fig. 8. It has been regularized by the simple expediency of limiting λ to be less than 0.95 . We observe that the plot of the rate at the front is approximately

linear on a log-log scale. This indicates that the $\mathsf{d}P_s/\mathsf{d}x$ factor from Eq. (14) dominates the expression for the rate in Eq. (11). Moreover, from the Pop plot for PBX 9501, $b = 0.51$, and the pressure exponent is $1 + 1/b = 3$. This is nearly the slope of the front rate shown in fig. 8.

It is important to note that the derived rate depends in part on the choice of EOS model. For example, the PBX 9501 rate shown in fig. 8 is about 3 times larger near the CJ pressure than the rate for PBX 9404 shown in [Mader, 1998, fig. 4.6, p. 199]. PBX 9404 has a similar high HMX content to PBX 9501, but due to a different binder is more sensitive at shock pressures below 10 GPa. The difference in the Forest fire rates is partly due to the Pop plots shown in fig. 5 and partly due to the EOS models.

The measured reaction zone profile for PBX 9501 has the form of a classical ZND detonation [Gustavsen et al., 1998a,b]. Also shown in fig. 8 is the chemical rate based on reactant shock temperature from an EOS model and Arrhenius rate parameters compatible with the measured CJ wave profile [Menikoff, 2006]. We note that below the CJ pressure, the bulk chemical rate is less than the Forest fire rate. This is an indication that reaction is dominated by hot spots. However, at the von Neumann (VN) spike state, the chemical reaction is sufficiently large to dominate a steady propagating detonation wave. In this regard, PBX 9501 may be an exceptional case because its high HMX content leads to a large detonation velocity and consequently the VN spike temperature is higher than for other PBXs. The increased detonation velocity has a large effect on the bulk rate since the chemical rate is very sensitive to temperature

5.2 Gradients behind shock front

In numerical simulations, as noted by Lunstrom [1988] and discussed in sec. 7, the gradients behind the lead shock front become large as a detonation wave is approached. Large gradients are also observed in velocity gauge data for PBX 9501 shown in fig. 9. We note that by the last gauge, the wave has transited to a detonation. The peak velocity is nearly the same as the CJ state velocity (2.17 km/s) of PBX 9501 based on the EOS. Velocity Interferometry System for Any Reflector (VISAR) measurements with high temporal resolution (1 ns) show a VN spike velocity (3.55 km/s) matching that computed from the EOS [Gustavsen et al., 1998a,b, Fedorov, 2002, Menikoff, 2006]. The gauge record is an example in which limited resolution, from the response time of the gauge, gives the appearance of a reactive shock.

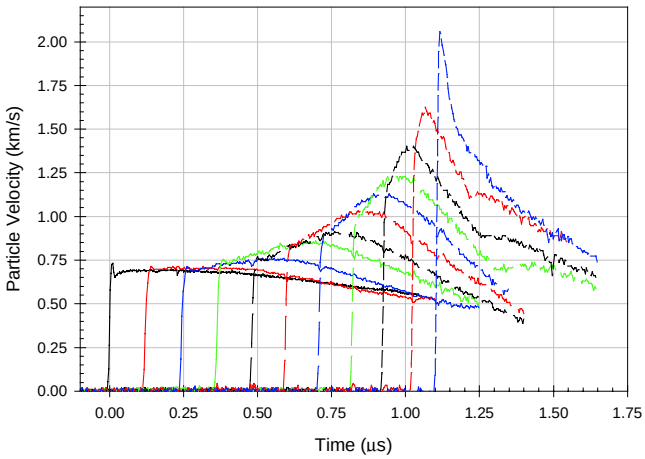

Figure 9: Lagrangian velocity time histories for shock initiation of PBX 9501 at input pressure of 5.15 GPa. The initial positions are 0.5 mm apart. Magnetic velocity gauge data is from Gustavsen et al. [1999, fig. 6]; reproduced with permission of the authors. The x–t trajectory for the same experiment is shown in fig. 3.

The velocity gauge data determines the particle acceleration, $\mathsf{d}u/\mathsf{d}t$, behind the shock front. This can be used to correct the rate at the shock front by accounting for the gradients in the flow. The relative effect on the rate, equations (11)–(13), from the flow gradients is characterized by the quantity g. It can be split into two factors; one from the EOS and a second from the ratio of the particle acceleration to the shock acceleration. For our PBX 9501 example, these quantities are shown in fig. 10. We observe that the ratio of the accelerations is less than two and that the EOS factor is less than about 0.25 . Consequently, g can be as large as 0.5 . Hence, the flow gradients can lower the rate at the front by up to 50 %. However, due to the numerical implementation of the Forest fire model, as discussed in sec. 7, simulations display significantly smaller gradients than those inferred from the velocity gauge data. Moreover, as noted earlier, the lead EOS factor is $z^2-1=(z+1)(c+u-u_s)/(u_s-u)$. Thus, the effect of the flow gradients on the rate is suppressed when the flow behind the shock front is nearly sonic.

In addition, we observe from the velocity gauge data shown in fig. 9 that at early times ($t \lesssim 0.75\,\mu$s) the lead shock velocity tracks the envelope of the previous velocity gauges. This implies that the particle acceleration is

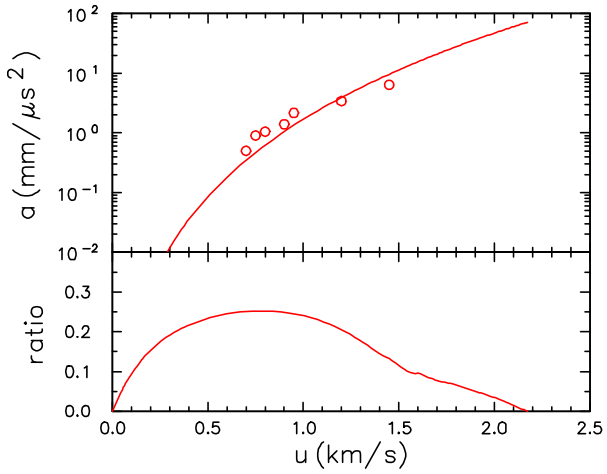

Figure 10: Effect of pressure gradient on reaction rate for PBX 9501. Top plot is the acceleration of shock front, $V_0\,\mathsf{d}P_s/\mathsf{d}x$, from the Pop plot. Symbol are particle acceleration $\mathsf{d}u/\mathsf{d}t$ behind the shock front estimated from the velocity gauge data shown in fig. 9. Bottom plot is the equation of state factor in g (first two factors in Eq. (13)) for the contribution of the gradient term on the rate, Eq. (12). The x-axis is the particle velocity along the Hugoniot locus.

about the same as that from the shock acceleration, *i.e.*, $\frac{\mathsf{d}u}{\mathsf{d}t} \approx \frac{\mathsf{d}u}{\mathsf{d}t_s}$. We can use this approximation to estimate g. By replacing $\frac{\mathsf{d}P_s}{\mathsf{d}x}$ with $\frac{\mathsf{d}u}{\mathsf{d}t_s}$, Eq. (13) can be expressed as

$$g = \left[\frac{z^2-1}{1+\frac{u}{u_s}\frac{\mathsf{d}u_s}{\mathsf{d}u}+z^2}\right]\left[\frac{\mathsf{d}u/\mathsf{d}t}{\mathsf{d}u/\mathsf{d}t_s}\right] \quad .$$

Consequently, the first factor, which depends only on the EOS, is a reasonable estimate for the relative effect of the gradients on the rate.

The velocity gauge data provides more information than just the slope behind the lead shock. This is discussed further at the end of sec. 7. Here we note that Lagrangian analysis have been applied to gauge data; see [Forest et al., 1989]. Incorporating the rate at the front from Pop-plot data and the Forest fire analysis should improve the accuracy of the Lagrangian analysis.

In principle, even without velocity gauge data, the flow gradient can be accounted for in a self-consistent manner with an iterative scheme. Neglecting the gradients, *i.e.*, starting with $\mathcal{R}_0$, can be consider as an initial approximation for the Forest fire rate $\mathcal{R}_{\rm FF}$. This can be used in a numerical simulation

of a shock-to-detonation transition to compute the gradients behind the front as a function of shock pressure. Then $\partial_x P = -\rho \frac{\mathsf{d}u}{\mathsf{d}t}$ can be used in equations (12) and (13) to determine a better approximation for $\mathcal{R}_{\mathrm{FF}}$. In practice this has not done.

The analysis of the effect of the flow gradients provides insight into the single-curve buildup principle. If $g \ll 1$, then the rate at the shock front totally dominates the shock acceleration. Even when only small, say $g \lesssim \frac{1}{2}$, the flow gradients immediately behind the front may be largely determined by the reaction initiated by the shock front. This is consistent with the idea that the lead shock activates hot spots at nucleation sites (*e.g.*, pores associated with porosity in a PBX), which then burn on a fast enough time scale to be unaffected by flow gradients. In either case, the shock trajectory would be independent of the driving conditions.

The flow gradients may be important for insensitive explosives, in which the rate does not dominate the behavior of the shock front. If the gradients are important for determining the rate then the single-curve buildup principle should break down, in which case the Pop plot would depend on the initiation system. There is, however, the possibility that the single-curve buildup would still appear to hold. To illustrate this point, suppose the buildup curve is identified with the shock trajectory from a low pressure initiation experiment with a long run-to-detonation distance. If higher pressure wedge experiments have an initial pressure gradient, from the explosive drive system, close to that of the buildup curve at the corresponding pressure, then the shock trajectories would be, to a good approximation, the same as the buildup curve. Hence, the single-curve buildup principle would appear to be valid, even though for other experiments the flow gradient could have a significant effect.

5.3 Shock dynamics

There is an interesting analogy to Whitham-Chisnell shock dynamics [see Whitham, 1974, sec. 8.1] for a shock wave propagating in a duct with variable cross sectional area. A source term arises in the characteristic equations from the change in area. Thus, $\mathsf{d}A/\mathsf{d}x$ plays a role analogous to the reaction rate. For duct flow, the source term is specified and the forward characteristic equation determines the shock strength as a function of area. The Forest fire model, on the other hand, uses the forward characteristic equation in the reverse manner; the shock strength is given and used to determine the source

term, *i.e.*, the reaction rate.

Compared to the Guderley solution, shock dynamics is a very good approximation for a converging shock. This is because the converging shock front accelerates and outruns interactions generated by the backward characteristics. Similarly, reaction accelerates a shock wave. Moreover, the state behind a reactive shock is approaching the sonic condition (CJ state) which would decouple the reaction zone from the flow behind. The Guderley solution has a limiting characteristic which plays an analogous role to the sonic condition for a detonation wave.

The exact Guderley solution requires that the far boundary condition is compatible with the similarity solution. However, independent of the boundary condition, a converging shock asymptotically approaches the portion of the Guderley solution between the shock front and the limiting characteristic. The single-curve buildup principle plays an analogus role to the limiting characteristic of the Guderley solution for a converging shock. This provides some intuition for a key assumption of the Forest fire model.

6 Implementation issues

Key issues for implementing the Forest fire model are related to the singularity in the derived rate at the CJ pressure, and to the assumption of a reactive shock. These issues are discussed next.

6.1 Fitting form for rate

In the original Forest fire model, Mader and Forest [1976] fit $\ln[\mathcal{R}_{\rm FF}(P)]$ to a polynomial in P with up to 14 coefficients. We note from fig. 1B and fig. 8 that both λ and $\ln \mathcal{R}$ are smooth functions of P. In fact, as discussed previously, $\mathcal{R}(P)$ is nearly linear on a log-log plot. Moreover, $\mathcal{R} \approx \text{constant} \times P^n$ with $n \approx 1 + 1/b$ where b is the slope of the Pop plot. Rather than a high order polynomial, it would be better to fit λ and $\mathcal{R}/P^n$ separately to low order polynomials and express the Forest fire rate as a rational function

$$\mathcal{R}_{\rm FF}(P) = \mathcal{R}(P)/[1 - \lambda(P)] \ . \tag{15}$$

Alternatively a cubic spline could be used to fit $\mathcal{R}_{\rm FF}$. Splines are now a well developed method for approximating functions, and are efficient to evaluate.

At $\lambda = 1$, Eq. (15) is singular. One way to regularize $\mathcal{R}_{\mathrm{FF}}$ is to apply a cutoff; for example, to replace λ with $\min(0.95, \lambda)$. In fact, to avoid difficulties with incomplete burn, codes typically burn the remainder of any cell with λ above a cutoff of about 0.95; see for example [Mader, 1998, p. 197] or [Shaw and Straub, 1981, pp. 215–220].

Another way to regularize $\mathcal{R}_{\mathrm{FF}}$ is to modify the reactive Hugoniot locus such that the CJ pressure corresponds to a smaller wave speed than the CJ detonation speed. For a linear u_s–u_p relation, this amount to using a smaller value of s than $(D_{\mathrm{CJ}} - c_0)/u_{\mathrm{CJ}}$, which results in a higher compression ratio for a given shock pressure. Combined with extending the Pop plot and applying Eq. (12), the rate can be extended slightly beyond P_{CJ}. It is important to note that neither Hugoniot data nor Pop-plot data extend up to the CJ pressure. Therefore, any regularization is necessarily *ad hoc*.

The factor $1 - \lambda$ in Eq. (2) would correspond to a first order reaction for a homogeneous material. For a heterogeneous explosive, the reaction rate is due to hot spots, and an ignition and growth burn mechanism is plausible. In this case, reaction is dominated by deflagration fronts triggered by hot spots. The dependence of the rate on the reaction progress variable can then be associated with the area of the burn front; for example, $\lambda^{2/3}$ for outward hole burning or $(1 - \lambda)^{2/3}$ for inward grain burning. We note that the exponent for grain burning is less than 1. Consequently, a steady wave would have a finite reaction zone width. This is in contrast to a first order reaction which has an exponential tail. Modifying the reaction order used for the Forest fire rate has been suggested by Starkenberg [1993, p. 999]. As discussed in later sections, the reaction order can be used as fitting a parameter to obtain better agreement with either the curvature effect or velocity gauge data.

6.2 Reactive shock profile

The Forest fire model was developed and has been used in hydro codes with a shock capturing algorithm based on artificial viscosity. The typical implementation introduces an inconsistency with the derived rate. Namely, the Forest fire rate assumes a discontinuous reactive shock with a value of λ at the shock front from a specified reactive Hugoniot locus, while the code implementation allows burning within the numerical shock profile and does not constrain λ to be on the reactive locus at the end of the shock profile. This inconsistent treatment of the reactive shock can have a significant effect on the rate at the shock front due to the $1 - \lambda$ multiplier in Eq. (15).

In contrast to a ZND wave profile, a steady detonation wave for the Forest fire model, as implemented in a hydro code, has a continuous profile usually associated with a weak detonation. A continuous profile is an implicit requirement of the Forest fire model since the derivation of the rate leads to a domain well below the VN spike pressure.

The standard operating procedure for simulations with the Forest fire model is to tune the viscous coefficient on the grid being used such that a planar steady detonation wave profile ends at the CJ state rather than a point on the weak branch of the detonation locus. In addition, for Lagrangian algorithms, the reaction rate is typically taken to be a function of the stress, *i.e.*, sum of the pressure plus the viscous pressure; see for example, [Shaw and Straub, 1981, p. 219]. This has two important consequences. First, the model depends on the form of the numerical dissipation used for shock capturing, and hence the solution is implementation dependent. Second, the viscosity must be adjusted with the cell size in order for the solution to converge under mesh refinement. Since the choice of the viscous coefficient is imprecise, convergence studies would be somewhat subjective.

In addition, the Forest fire model was developed in the 1970s when the available computing power limited the mesh resolution that could be used. The cell size, in effect, introduced a length scale which can have a significant effect on the results of a simulations. In order for the Forest fire model to be well posed, the dissipation required for the detonation profile needs to be included as an integral part of the model. We suggest utilizing a viscous pressure analogous to the von Neumann-Richtmyer artificial viscosity. Namely, to replace P in the reactive flow equations (1) with $P+Q$, and choose for the viscous pressure

$$Q = -\nu\rho \left[c + r \left| \ell \frac{\mathsf{d}u}{\mathsf{d}x} \right| \right] \ell \frac{\mathsf{d}u}{\mathsf{d}x} \ , \tag{16}$$

where ν is a dimensionless viscous coefficient, r is the ratio of quadratic to linear viscous terms, and ℓ is a length scale.

The continuum mechanics viscosity can be reduced to the usual form of numerical artificial viscosity by taking ℓ to be the cell size and replacing $\ell \frac{\mathsf{d}u}{\mathsf{d}x}$ with Δu, *i.e.*, the velocity difference across a cell.[6] The effective coefficient

[6]Modern shock capturing algorithms aim at minimizing the number of cells in the numerical shock profile. One method for Eulerian algorithms is to construct a piecewise linear velocity from the values of velocity at the cell centers, then to replace Δu in the

of dynamic viscosity[7] is proportional to $\nu\,\rho\,c\,\ell$. For an artificial viscosity, it decreases with grid resolution. The purpose is to provide sufficient dissipation for shock stability. In contrast, our motivation for using Eq. (16) is to introduce a length scale for the burn model in the continuum equations by relating ℓ to the reaction zone width independent of the computational cell size.

6.2.1 Detonation wave profile

It is instructive to analyze the detonation wave profile for the continuum PDEs. The general case, with viscosity, heat conduction and mass diffusion has been worked out; see Gasser and Szmolyan [1993] and references therein to earlier work. The problem is much easier when only viscosity is considered. In this case, it can be reduced to a system of only two ODE and the phase-plane can be readily visualized.

For a steady planar wave, the mass and momentum equations imply that

$$\Delta(P+Q) = -m^2\Delta V = m\Delta u \ , \tag{17}$$

and together with the energy equation imply that

$$\Delta e = (P_0/m + \tfrac{1}{2}\Delta u)\Delta u \ , \tag{18}$$

where $m = \rho_0(D-u)$ is the mass flux, and Δ denotes the change in a variable across the wave. When the material ahead of the wave is at rest and with Eq. (16) for the viscous pressure, the detonation wave profile is determined by the ODEs

$$\frac{\mathsf{d}}{\mathsf{d}\xi}u = -\frac{c}{2\,r\,\ell}\left[\left(1+4r\left|\frac{Q}{\nu\,\rho\,c^2}\right|\right)^{1/2} - 1\right]\mathsf{sgn}(Q) \ , \tag{19a}$$

$$\frac{\mathsf{d}}{\mathsf{d}\xi}\lambda = -\frac{\mathcal{R}(\lambda, P+Q)}{D-u} \ . \tag{19b}$$

Here $\xi = x - D\,t$ is the spatial coordinate in the frame moving with the wave, and D is the wave speed in the lab frame. The other variables are obtained

formula for Q by the discontinuity at the cell boundary. Alternatively, numerical dissipation can be introduced using approximate Riemann solvers for the flux at cell boundary, rather than with a viscous pressure.

[7] Dynamic viscosity has units of pressure $\times$ time.

from algebraic equations (17), (18) and the EOS:

$$
\begin{aligned}
V &= V_0 - u/m \ , \\
e &= e_0 + (P_0/m + \tfrac{1}{2}u)\, u \ , \\
P &= P(V, e, \lambda) \ , \\
Q &= m\, u - P + P_0 \ .
\end{aligned}
$$

The initial state, at $\xi = \infty$, is denoted by the subscript '0'.

In the (u, λ)-phase-plane, the weak and strong points on the detonation locus and the initial state[8] are fixed points for which the right hand side of Eq. (19) vanishes. For the analysis of the ODE trajectories, a key role is played by the loci in the phase-plane corresponding to the intersection in the (V, P)–plane of the Rayleigh line, $P - P_0 = m^2(V_0 - V)$, with the weak and strong branches of the partially burned Hugoniot loci. From Eq. (17), the Rayleigh line corresponds to $Q = 0$, and from Eq. (19a) to $\frac{\mathsf{d}}{\mathsf{d}\xi} u = 0$. Moreover, $\frac{\mathsf{d}}{\mathsf{d}\xi}\lambda \geq 0$ since the reaction rate $\mathcal{R} \geq 0$. It follows that in the phase-plane $\frac{\mathsf{d}u}{\mathsf{d}\lambda} > 0$ if and only if the state lies between the weak and strong branches of the the partially burned Hugoniot loci. As a consequence, the strong point on the detonation locus is a stable fixed point and the weak point is a saddle point. At the CJ detonation speed, the weak and strong points coincide. As a fixed point, the CJ state is stable for trajectories approaching from high pressure and unstable when trajectories approach from low pressure.

Example trajectories in the (u, λ)–plane and (V, P)–plane for PBX 9501 at CJ wave speed, as the viscosity coefficient ν is varied (with $\ell = 0.05\,\mathrm{mm}$ and $r = 0.5$), are shown in fig. 11. The trajectories vary with viscosity as follows:

(i) For small viscosity, there is a viscous shock profile to nearly the von Neumann spike state, followed by reaction along the Rayleigh line to the CJ state. This corresponds to the ZND profile.

(ii) For larger values of the viscosity, there is a competition between viscous and reactive time scales that results in a non-monotonic profile with peak pressure below the von Neumann spike pressure.

(iii) There is a unique value of the viscous coefficient such that the pressure within the wave profile to the CJ state is monotonic. It is natural to base

[8] To avoid the so called cold boundary problem, we assume a small cutoff pressure below which the rate vanishes. This is equivalent to assuming that the trajectory for the wave profile at the initial state has slope $\mathsf{d}\lambda/\mathsf{d}u = 0$.

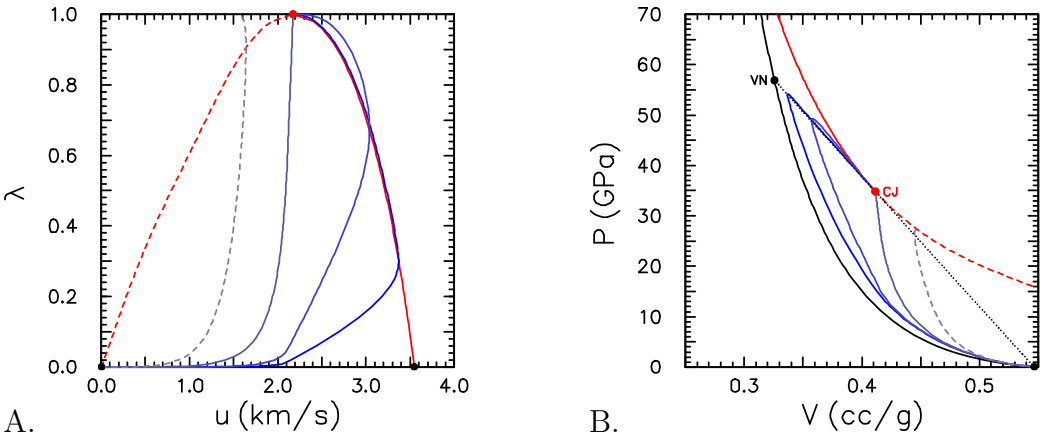

Figure 11: Phase plane for steady viscous detonation wave in PBX 9501 at CJ wave speed. Trajectories shown for viscosity of $\nu = 0.001$, 0.01, 0.35, 5 (varying with blue tint). Dashed line does not end at fixed point and hence does not correspond to steady profile. A. Red curve is image of Rayleigh line; dashed and solid are weak and strong branch, respectively. B. Black curve is unreacted shock locus, and red curve is detonation locus; dashed and solid are weak and strong branch, respectively. Dotted black line is Rayleigh line. Red and black symbols denote CJ and von Neumann spike states, shock.

the Forest fire model on this value for the viscosity.
(iv) For still larger values of the viscous coefficient, the trajectory crosses the weak branch of the Rayleigh line and does not end on the detonation locus. These trajectories are not valid steady state profiles. The solution to the time dependent PDEs for an underdriven wave, would have a lower detonation speed for which the detonation profile would end on the weak branch of the detonation locus.

The unique CJ detonation wave profile with a monotonic pressure is shown for PBX 9501 in fig. 12. The reaction zone width is an important quantity. To avoid the precursor tail we take the spatial origin — somewhat arbitrarily — to correspond to a pressure of 0.1 GPa. We note that the viscous pressure at the spatial origin is much larger, order of 1 GPa. With this choice, the width of the reaction zone for the Forest fire model is about 0.05 mm. This is comparable to the experimental value of 0.025 mm based on VISAR measurements; see [Menikoff, 2006] and references therein. For the Pop plot, on which the rate is based, the run distance at the CJ pressure is 0.13 mm. The model reaction width can be varied with the form of

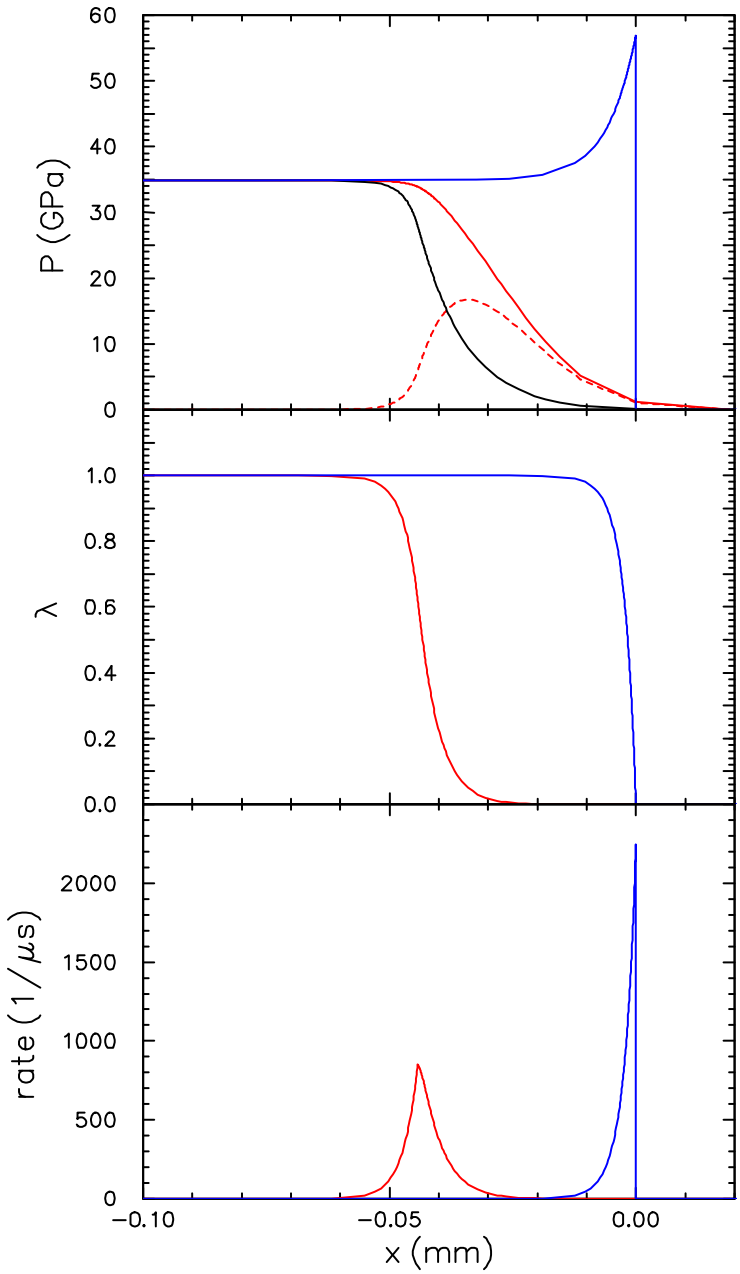

Figure 12: Detonation wave profile for PBX 9501. Red and blue curves correspond to Forest fire rate with viscous shock and discontinuous lead shock, respectively. For viscous profiles, spatial origin corresponds to pressure of 0.1 GPa. For the pressure plot, black, red and dashed red curves are P, $P + Q$ and Q, respectively.

the viscous pressure, such as parameter r in Eq. (16), or with the reaction order for the rate. This freedom can be used to adjust the magnitude of the curvature effect discussed in sec. 8.2.

Several remarks are in order:

(i) The Pop plot does not determine the steady reaction zone width. The distance of run extrapolated to the CJ pressure only gives an indication of a relevant length scale for the Forest fire model. For a reactive shock, the width would literally be zero. The actual width reflects an inconsistency between the reactive shock assumption and the implementation of the model with a continuous profile. Moreover, a shock capturing scheme can not distinguish the reaction in the shock profile from subsequent reaction that accelerates a reactive shock to a detonation wave. Because of the inconsistency between the assumption and implementation, the model will not reproduce the Pop plot exactly.

(ii) The viscous pressure Q peaks at $\lambda \approx 4\,\%$. Reaction in the shock rise is enhanced by taking the rate to be a function of $P+Q$, and is in keeping with the assumption of a reactive shock. If instead the rate in Eq. (19) is taken as a function of P, then the viscous coefficient needed for the unique monotonic detonation profile would be over an order of magnitude larger and the reaction zone width in excess of 1 mm. We note that the advection step in an Eulerian simulation is diffusive, and some implementations of the Forest fire model do use a rate as a function of P rather than $P + Q$.

(iii) Suppose one were to use only an artificial viscosity with fixed value of viscous coefficient. Then as the mesh is refined and the effective viscous coefficient decreased, the reaction zone profile would approach the ZND profile; blue curve in fig. 12. On the other hand, suppose both an artificial and continuum form of viscous pressure were used. Then on coarse meshes the artificial viscosity would dominate and a simulation would be similar to present implementations. But on fine meshes, when Eq. (16) dominates, the solution should converge to the continuum solution with the steady profile shown in fig. 12. It is important to note that when the continuum Q dominates the reaction zone, the PDEs would have a parabolic character. The stability criterion for an explicit algorithm would then be $\Delta t < (\Delta x)^2/(\nu\, c\, \ell)$ rather than the hyperbolic CFL condition, $\Delta t < \Delta x/c$. Consequently, either a very small time step or an implicit algorithm, such as backward Euler, would be needed on very fine meshes.[9]

[9]For an artificial viscosity, $\ell = \Delta x$, and the condition for a stable parabolic time step

Other forms of numerical dissipation have been used for shock capturing algorithms. In particular, Godonov algorithms use approximate Riemann solvers. On coarse meshes with a fast reaction rate, weak detonation waves with continuous profiles can occur in simulations; see Colella et al. [1986]. In contrast to artificial viscosity methods, the dissipation in a Godunov algorithm can be increased only a limited amount by reducing the scheme to first order. Consequently, under mesh resolution the solution for a steady detonation wave would converge to a ZND profile. Thus the original Forest fire model could only be applied with a Godonov scheme on coarse meshes. Explicitly, introducing a viscous dissipation into the Forest fire model enables the model to be well posed independent of the numerical dissipation used by a shock capturing algorithm.

One possible approach for introducing a consistent reactive shock with a shock capturing alorithm would be to construct an artificial rate that tracks the reactive Hugoniot on shock rise. This could be done as follows. Let $\lambda_r(P)$ denote the value of λ on the reactive shock Hugoniot as a function of pressure. Calculate $\mathsf{d}P/\mathsf{d}t$ and update λ with a modified rate,

$$\max\left[\mathcal{R}(\lambda, P), \frac{\mathsf{d}\lambda_r}{\mathsf{d}P} \cdot \frac{\mathsf{d}P}{\mathsf{d}t}\right] .$$

On a sufficiently fine mesh, the $\mathsf{d}P/\mathsf{d}t$ term should dominate in the shock profile, while the usual rate should dominate elsewhere. Naturally, this idea would require further study to test whether it works, or could be modified to work, on problems of interest.

Finally, we note that Starkenberg [1993] implemented the Forest fire model in a 1-D code with a true discontinuous reactive shock by tracking the lead front. Tracking is considerably more difficult in 2-D. In addition, there are issues with multiple shocks and the curvature effect, discussed in the next section, which would be difficult to overcome with front tracking.

7 Numerical example

To illustrate some of the properties of the Forest fire model we have run a shock-to-detonation simulation for PBX 9501. The calculation uses a Godunov algorithm with the continuum viscosity described in the previous section. The viscous reactive profile is resolved with an adaptive mesh. The

is proportional to the hyperbolic time step.

shock is driven by a piston with velocity of 0.7 km/s. This case corresponds to the gas gun experiment by Gustavsen et al. [1999] with shock trajectory and velocity gauge data shown in figs. 3 and 9.

The time evolution of pressure, particle velocity and burn fraction profiles are shown in fig. 13. Several features of the profiles are noteworthy: (i) Though the reaction zone profile is resolved numerically (finest grid with 5 μm cell size), on the 10 mm scale of the plot, the lead wave appears discontinuous. (ii) The pressure gradient behind the lead wave is fairly small up to a shock pressure of about half P_{CJ}, 15 GPa. But at higher shock pressures, there is a significant gradient. The rapid increase in shock pressure implies that the reactive source term dominates over the gradients for the transition to detonation. (iii) The rapid final stage of the transition to detonation is a transient. At the transition, the shock pressure exceeds the CJ pressure and then on the time scale of the reaction zone (10 ns) equilibrates to the CJ pressure. The pressure spike gives rise to a left propagating pulse in the reacting explosive, as seen in the subsequent pressure and velocity profiles. Moreover, this pulse is slower than the phase velocity for completion of the reaction in the partly reacted shocked material. (iv) Even for relatively weak shocks, there is a significant gradient in the particle velocity. The velocity gradient is a consequence of the shock acceleration, *i.e.*, the shock-change equation described in App. C.

Lagrangian velocity time histories are shown in fig. 14. We note that Lagrangian time histories are considerably different than the profiles at fixed time. Only for a steady wave would they be the same, up to a scale factor of the axes; $x/t = D$. Compared to the experimental measurement shown in fig. 9, shock arrival times at the gauges are in good agreement, because the model is calibrated to the Pop plot. But the shape of the profiles clearly differ. The velocity at late time is affected by the boundary condition. The piston boundary does not allow the explosive to expand against the experimental flyer plate as the pressure rises due to reaction. More important is the fact that the particle acceleration behind the shock front is significantly lower than that from the velocity gauge records. The gauges do perturb the flow. Nevertheless, the difference behind the shock front is larger than the expected experimental uncertainty.

There are two likely explanations for the discrepancy in the particle acceleration behind the shock. First is the fitting form used for the rate, in particular, the assumed λ dependence in Eq. (2). Second is the inconsistency discussed in sec. 6.2 between the discontinuous reactive shock assumed by

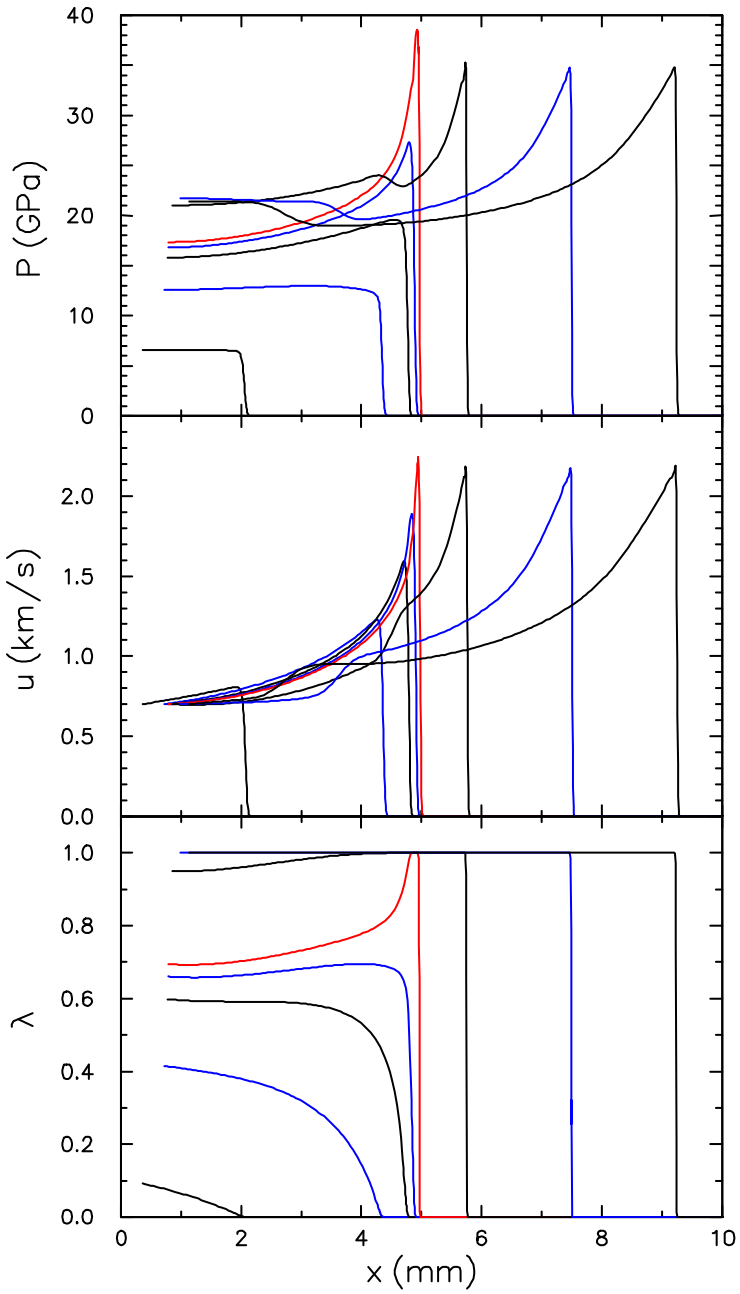

Figure 13: Evolution of P, u and λ profiles for shock-to-detonation transition in PBX 9501. Profiles are at $t = 0.5, 1.0, 1.08, 1.1, 1.11, 1.2, 1.4, 1.6\,\mu$s. Transition at $t = 1.11\,\mu$s is shown as red curve in each plot.

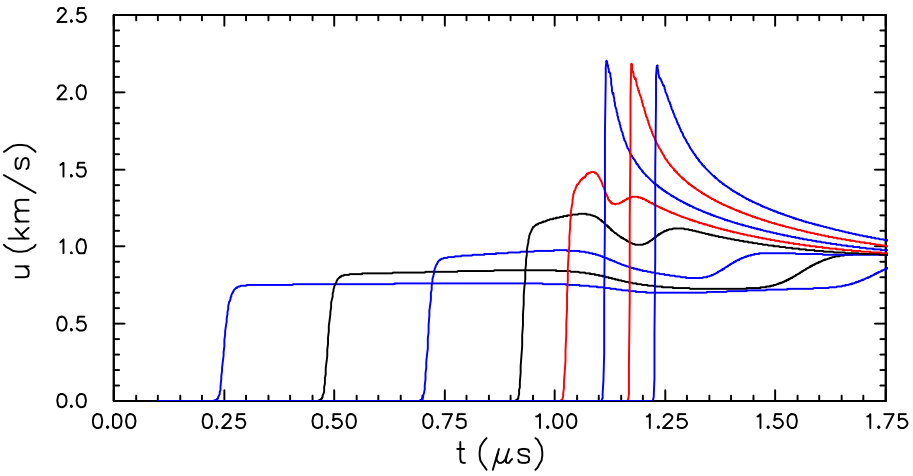

Figure 14: Simulated Lagrangian velocity time histories for shock-to-detonation transition in PBX 9501. The initial positions are at $x_0 = 1, 2, 3, 4, 4.5, 5, 5.5, 6$ mm.

the model and the reactive shock profile employed in numerical implementations. A consequence of the small numerical particle acceleration is that calibrating the Forest fire rate using Eq. (11), *i.e.*, with the zero pressure gradient assumption, is compatible reproducing the Pop plot.

This example illustrates a strength and weakness of the Forest fire model. An advantage of the model is that only limited data — Pop plot and reactive Hugoniot — are needed to calibrate the rate. The flip side is that the model has no degrees of freedom to fit profile data empirically. Based on the simplifying model assumption, that the global rate has the same functional form as it does at the front, there is no reason to expect good agreement with gauge data, which is affected by the rate behind the front.

A Lagrangian analysis can be used to relate the rate behind the front to velocity gauge data; see for example Forest et al. [1989]. Alternatively, better agreement with the velocity gauge data may be obtained by utilizing a more general fitting form for the rate, such as assuming $\mathcal{R} = (1-\lambda)^n \mathcal{R}_{\rm FF}(P)$ with $0 < n < 1$, *i.e.*, the rate is not first order in λ. Other burn models, such as Ignition and Growth [Lee and Tarver, 1980] use a rate of this form. Moreover, from a detailed examination of the profiles in fig. 13, as the wave builds up to a detonation most of the burning occurs behind the front. Consequently, a reactive shock and monotonic or weak detonation profile are not essential

for matching the front trajectory in a shock-to-detonation transition; see for example [Lambert et al., 2006, sec. 3]. However, the analysis used to derive the Forest fire rate would apply and determine the rate at the front needed for compatibility with Pop-plot data, whether or not the lead shock is reactive.

8 Model limitations

Simplified burn models have their limitations. Inaccuracies result from tacit assumptions on the hot-spot distribution and an overly large reaction zone width from lack of resolution. These points are briefly discussed next.

8.1 Shock desensitization

The Forest fire rate is calibrated to Pop-plot data, *i.e.*, shock-to-detonation transition experiments. Hence it assumes a hot-spot distribution from a single shock. Other experiments demonstrate that the hot-spot distribution is affected by the flow. A notable example is shock desensitization, in which a weak shock can quench a propagating detonation wave [Campbell and Travis, 1986]. For a PBX, ignition is sensitive to small amounts of porosity. Presumably, a weak shock can close pores and eliminate potential nucleation sites for hot spots from subsequent waves. A rate that depends only on pressure, can not account for this effect.

Simple burn models can be extended by adding another variable to keep track of the lead shock strength as a function of position, and then adjusting the rate based on the lead shock strength. One such model is multiple-shock Forest fire, see [Mader, 1998, sec. 4.3] and [Mader et al., 2002]. An algorithm for a shock pressure variable can be based on the artificial viscous pressure which peaks within a numerical shock profile. The Forest fire rate is then limited to a value corresponding to the lead shock pressure. In effect, the rate is a function of an additional internal state variable; $\mathcal{R}(\lambda, P, P_s)$. For a more detailed discussion of burn models motivated by hot spots and the dependence of the burn rate on lead shock pressure see Johnson, Tang, and Forest [1985], in particular, their discussion around Eqs. (19) and (20).

We note that the general Forest fire analysis yields the rate at the shock front required for the shock strength to increase in accordance with the Pop plot. Any burn model can be used as a functional form for the reaction rate away from the shock front. The rate at the shock provides an important

constraint on model parameters.

Several other experiments show that the flow affects the hot-spot distribution, and hence the rate. Noteworthy is the 2-D flow that arises from detonation diffraction, often referred to as corner turning, which leads to a pocket of unreacted HE called a dead zone; see [Souers et al., 2004] and references therein. Pressure dependent rates alone are not sufficient to reproduce sustained dead zones; see [DeOliveria et al., 2006].

Isentropic compression techniques have been developed for high pressure equation of state measurements; see [Hooks et al., 2006, Baer et al., 2006]. Due to the absence of dissipation from shock heating, isentropic compression would generate fewer and weaker hot spots than shock compression to the same pressure. Consequently, the Forest fire rate would over-predict the reaction rate for isentropic compression, or more generally when a ramp pressure rather than a shock is applied to an HE; see [Starkenberg, 1993].

8.2 Curvature effect

Though the CJ detonation velocity is the minimum wave speed for a planar detonation wave, rate stick experiments [Campbell and Engelke, 1976] have shown that curved detonation waves have a lower detonation velocity. Donguy and Legrand [1981] have performed simulations of rate sticks with the Forest fire model and compared with experiments using a PBX composed of 95.5 wt % TATB and 4.5 wt % VITON. They find on coarse meshes that the simulations display a diameter effect (variation of detonation velocity with rate stick diameter) larger than the experimental measurements. The numerical diameter effect appears to converge to the experimental value as the mesh is refined. They do not, however, specify the form of artificial viscosity used or how the viscous coefficient is adjusted with cell size.

Over predicting the diameter effect is a generic problem for simulations when the reaction zone is not sufficiently resolved. It can be explained as follows. The reaction zone width and front curvature together lead to modified jump conditions for a quasi-steady detonation wave, see Menikoff et al. [1996, Eq. (5.1–3)]:

$$\begin{aligned} \Delta[\rho(D-u)] &= \kappa w \, \langle \rho u \rangle \ , \\ \Delta \left[\Big(\rho(D-u) \Big)^2 V + P \right] &= \kappa w \, \langle \rho(D-u) u \rangle \ , \\ \Delta \left[e + PV + \tfrac{1}{2}(D-u)^2 \right] &= 0 \ , \end{aligned} \tag{20}$$

where $\Delta[f] = f(x_0) - f(x_1)$ is the change of variable f across the detonation wave, $w = x_0 - x_1$ is the reaction zone width, κ is the front curvature, and $\langle f \rangle = w^{-1} \int_{x_1}^{x_0} \mathsf{d}x\, f$ is the average value of f in the reaction zone. For a planar front, $\kappa = 0$ and Eq. (20) reduces to the standard Rankine-Hugoniot jump conditions. On a coarse mesh, the reaction zone is not resolved and the reaction zone width will be artificially large. Since the right hand side of the jump conditions, Eq. (20), is proportional to κw, a conservative scheme can not distinguish between an artificially large w and a large κ, and therefore will over predict the effect of curvature.

We note that the right hand side of Eq. (20) is also proportional to average quantities within the reaction zone. Compared to other burn models with a ZND reaction zone profile, the average quantities will be lower for the typical implementation of the Forest fire model since the density ρ increases monotonically from the initial state rather than decreasing monotonically from the von Neumann spike state. The smaller average quantities can compensate for a larger reaction zone width. Thus, the Forest fire model can give rise to the same curvature effect as other models having a smaller reaction zone width.

Moreover, the reaction order of the rate affects the reaction zone width. The reaction order for a heterogeneous explosive can be viewed as a parameter related to the area of a burn front resulting from a hot spot. It can be adjusted to better fit data on the curvature effect; see for example [Lambert et al., 2006, sec. 3]. Comparison with velocity gauge data can then be used as a consistency check.

Two additional points are worth noting. First, a tracked reactive shock, as Starkenberg [1993] implemented in a 1-D code, would have a zero reaction zone width and hence the conservation laws would imply the absence of a curvature effect. Possibly, the curvature effect could be obtained utilizing a partly resolved reaction zone [Bdzil and Davis, 1975] in which the tracked reactive shock models a fast reaction for the bulk of the burn fraction and then the final slow reaction for the remainder of the burn fraction is resolved. Second, for just propagation of a detonation wave, the Detonation Shock Dynamics (DSD) model can be used; see [Bdzil and Stewart, 1989, Aslam et al., 1996]. The model incorporates the curvature effect; detonation velocity as a function of local front curvature, $D(\kappa)$. Since DSD assumes a quasi-steady detonation wave, it is not suitable for initiation problems, which are inherently transient in nature.

9 Concluding remarks

Compared to other burn models, a distinguishing property of the Forest fire model (as usually implemented) is that the reaction zone for a steady detonation has a continuous profile, usually associated with a weak detonation, rather than a ZND profile. The Forest fire model is aimed at solid explosives, in particular plastic-bonded explosives. One might expect that the detonation front would be irregular due to heterogeneities within the explosive, and a homogenization based on averaging hydrodynamic variables transverse to the direction of wave propagation to give a smooth profile.

Some experiments do show front irregularities from hot spots, see for example [Plaksin et al., 2002] and references therein. Other experiments have measured the reaction zone of high HMX content PBXs, such as PBX 9501, using a velocity interferometry technique [Gustavsen et al., 1998a,b, Fedorov, 2002]. Their data displays a ZND profile which is compatible with an Arrhenius reaction rate based on bulk shock heating [Menikoff, 2006]. The VISAR spot size for the high resolution measurements is a fraction of a mm or a few times the average grain size. Other experimental techniques using the light intensity from a shock front [Loboiko and Lubyatinsky, 2000] give information on the average behavior of the reaction zone. However, the nature of the averaging is not clear. Determination of a homogenized or average profile would require high resolution data (1 ns temporal resolution and 10 μm spatial resolution) over a mm wide region of the detonation front. Until such data becomes available, despite the derivation for the reaction rate, Forest fire should be regarded as an empirical model.

The Forest fire rate is calibrated to Pop-plot data or shock initiation experiments on distance-of-run to detonation. Other empirical models can fit Pop-plot data; see for example [Starkenberg et al., 2006]. To objectively compare Forest fire with other models, one first has to eliminate the implementation dependence. To this end we proposed in sec. 6.2 incorporating a dissipative mechanism needed to get a well defined reaction zone profile directly in the Forest fire model.

Comparisons among models should also be done with mesh converged solutions. Coarse mesh solutions are of practical importance, but the mesh size needed for a desired accuracy should be a separate issue. However, resolution and model predictions may be coupled if model parameters are empirically fit based on coarse mesh solutions. As discussed in sec. 8.2, the numerical reaction zone width affects propagation of curved detonation

waves. The steady CJ reaction zone width of a model is the critical length scale for setting the numerical resolution.

Finally, we note that the Pop plot for a given explosive depends on the initial temperature, since an explosive is more sensitive when hot than cold. Simple burn models can not account for such changes in sensitivity. Typically, different rate calibrations are used for a hot and a cold explosive. In effect, a hot and a cold explosive of the same material are modeled as different explosives. Similarly, a PBX is more sensitive when pressed to low density than to high density. The variation of the Pop plot with pressing density has been analyzed by Forest [1978]. Different Pop plots could also be used for a precompressed PBX to describe shock desensitization. On the other hand, damage can introduce porosity and sensitize a PBX. One needs to be cognizant of these limitation when using a model to predict the behavior of an explosive for a new application. This is particularly relevant to accident scenarios since an explosive can be subjected to a wider variety of initiation stimuli over longer time scales than the design mode for which model parameters are calibrated.

Acknowledgments

This work was carried out under the auspices of the National Nuclear Security Administration of the U.S. Department of Energy at Los Alamos National Laboratory under Contract No. DE-AC52-06NA25396.

Appendix A. Equilibrium EOS derivatives

The ODE for the reactive Hugoniot locus, Eq. (5), requires partial derivatives of the mixture EOS. For the pressure-temperature equilibrium EOS, the pressure derivatives can be expressed in terms of the derivatives of the components after the equilibrium equations (3) are solved for the component states, (V_i, e_i). The equilibrium equations are equivalent to minimizing the Helmholtz free energy

$$F(V,T) = \lambda_1 F_1(V_1,T) + \lambda_2 F_2(V_2,T) \ ,$$

or maximizing the entropy

$$S(V,e) = \lambda_1 S_1(V_1,e_1) + \lambda_2 S_2(V_2,e_2) \ .$$

The resultant mixture EOS is complete and thermodynamically consistent, provided that the component EOS are thermodynamically consistent.

We first consider partial derivatives at fixed λ. It can be shown that the mixture isothermal sound speed is determined by

$$\frac{1}{(\rho\, c_T)^2} = \frac{\lambda_1}{(\rho_1\, c_{T1})^2} + \frac{\lambda_2}{(\rho_2\, c_{T2})^2}\ .$$

The specific heat $C_V = \left(\frac{\partial e}{\partial T}\right)_V$ and the Grüneisen coefficient $\Gamma = V\left(\frac{\partial P}{\partial e}\right)_V$ can be expressed as

$$\begin{aligned} C_V &= \lambda_1 C_{V1} + \lambda_2 C_{V2} + \frac{w_1 w_2}{w_1 + w_2}\left[C_{V1}\tfrac{\Gamma_1}{V_1} + C_{V2}\tfrac{\Gamma_2}{V_2}\right]^2 T\ , \\ \frac{\Gamma}{V} &= \frac{w_1 C_{V1}\frac{\Gamma_1}{V_1} + w_2 C_{V2}\frac{\Gamma_2}{V_2}}{(w_1+w_2)C_V}\ , \end{aligned}$$

where $w_i = \frac{\lambda_i}{(\rho_i c_{Ti})^2}$. Then the isentropic sound speed is given by the general thermodynamic relation

$$(\rho c)^2 = -(\partial_V P)_e + P(\partial_e P)_V = (\rho\, c_T)^2 + \left(\frac{\Gamma}{V}\right)^2 C_V T\ .$$

To determine $(\partial_\lambda P)_{V,e}$ consider the reactants and products variables to be functions of λ; *i.e.*, $V_i(\lambda)$, $e_i(\lambda)$ for $i = 1, 2$. Taking $\mathsf{d}/\mathsf{d}\lambda$ of Eq. (3) leads to a system of 4 simultaneous equations for $\mathsf{d}V_i/\mathsf{d}\lambda$ and $\mathsf{d}e_i/\mathsf{d}\lambda$. Then $\partial_\lambda P = (\partial_V P_1)\mathsf{d}V_1/\mathsf{d}\lambda + (\partial_e P_1)\mathsf{d}e_1/\mathsf{d}\lambda$. After some algebra one obtains

$$\frac{\partial P}{\partial \lambda} = \frac{\lambda_1 \delta P_1 J_2 + \lambda_2 \delta P_2 J_1}{\Delta}\ ,$$

where

$$\begin{aligned} \delta P_i &= (V_1 - V_2)(\partial_V P_i)_e + (e_1 - e_2)(\partial_e P_i)_V\ , \\ J_i &= (\partial_V T_i)_e(\partial_e P_i)_V - (\partial_e T_i)_V(\partial_V P_i)_e\ , \\ \Delta = &\quad \Big[\lambda_1(\partial_V T_2)_e) + \lambda_2(\partial_V T_1)_e)\Big]\Big[\lambda_1(\partial_e P_2)_V) + \lambda_2(\partial_e P_1)_V)\Big] \\ &- \Big[\lambda_1(\partial_V P_2)_e) + \lambda_2(\partial_V P_1)_e)\Big]\Big[\lambda_1(\partial_e T_2)_V) + \lambda_2(\partial_e T_1)_V)\Big]\ . \end{aligned}$$

Appendix B. Characteristic equations

The first step in deriving the characteristic equations for reactive flow is to re-express Eq. (1) in Lagrangian form:

$$\frac{\mathsf{d}V}{\mathsf{d}t} - V\partial_x u = 0 \ , \tag{21a}$$

$$\frac{\mathsf{d}u}{\mathsf{d}t} + V\partial_x P = 0 \ , \tag{21b}$$

$$\frac{\mathsf{d}e}{\mathsf{d}t} + PV\partial_x u = 0 \ , \tag{21c}$$

$$\frac{\mathsf{d}\lambda}{\mathsf{d}t} = \mathcal{R} \ , \tag{21d}$$

where $\frac{\mathsf{d}}{\mathsf{d}t} = \partial_t + u\partial_x$ is the convective time derivative. From Eq. (21a) and Eq. (21c), the energy equation can be express as

$$\frac{\mathsf{d}e}{\mathsf{d}t} + P\frac{\mathsf{d}V}{\mathsf{d}t} = 0 \ . \tag{22}$$

For a pressure-temperature equilibrium EOS, the mixture entropy is

$$S = \lambda_1 S_1 + \lambda_2 S_2 \ ,$$

and the fundamental thermodynamic identity in differential form is

$$\mathsf{d}e = -P\,\mathsf{d}V + T\,\mathsf{d}S + (\Delta G)\,\mathsf{d}\lambda \ , \tag{23}$$

where $\Delta G = G_2 - G_1$, $G = e + P\,V - T\,S$ is the Gibbs free energy and the subscripts 1 and 2 denote the reactants and products, respectively. Substituting into Eq. (22) leads to the entropy equation

$$T\frac{\mathsf{d}S}{\mathsf{d}t} = -(\Delta G)\frac{\mathsf{d}\lambda}{\mathsf{d}t} = -(\Delta G)\,\mathcal{R} \ . \tag{24}$$

Both the entropy equation (24) and the reaction equation (21d) are in characteristic form.

To obtain the acoustic characteristics, we begin by transforming the independent thermodynamic variables from (ρ, S) to (P, S). In differential form,

$$\mathsf{d}P = c^2\,\mathsf{d}\rho + (\partial_S P)_{V,\lambda}\,\mathsf{d}S + (\partial_\lambda P)_{S,\lambda}\,\mathsf{d}\lambda \ ,$$

where $c^2 = (\partial_\rho P)_{S,\lambda}$ is the square of the frozen sound speed. Utilizing Eq. (24), the time derivative of the pressure is

$$\frac{\mathsf{d}P}{\mathsf{d}t} = c^2 \frac{\mathsf{d}\rho}{\mathsf{d}t} + \Big[-(\partial_S P)_{V,\lambda} \frac{\Delta G}{T} + (\partial_\lambda P)_{V,S} \Big] \frac{\mathsf{d}\lambda}{\mathsf{d}t} \ .$$

From Eq. (23), it can be shown that the term in square brackets is equal to $(\partial_\lambda P)_{V,e}$. Therefore,

$$\frac{\mathsf{d}P}{\mathsf{d}t} = c^2 \frac{\mathsf{d}\rho}{\mathsf{d}t} + (\partial_\lambda P)_{V,e} \mathcal{R} \ .$$

Utilizing Eq. (21a) to eliminate the derivative of ρ, we obtain

$$\frac{\mathsf{d}P}{\mathsf{d}t} + \rho c^2 \, \partial_x u = (\partial_\lambda P)_{V,e} \mathcal{R} \ . \tag{25}$$

Linear combinations of Eq. (21b) and Eq. (25) lead to the characteristic equations for the acoustic modes:

$$\Big(\mathsf{d}/\mathsf{d}t + c\,\partial_x\Big)P + \rho c\Big(\mathsf{d}/\mathsf{d}t + c\,\partial_x\Big)u = (\partial_\lambda P)_{V,e}\mathcal{R} \ , \tag{26a}$$

$$\Big(\mathsf{d}/\mathsf{d}t - c\,\partial_x\Big)P - \rho c\Big(\mathsf{d}/\mathsf{d}t - c\,\partial_x\Big)u = (\partial_\lambda P)_{V,e}\mathcal{R} \ . \tag{26b}$$

The dimensionless quantity $(\partial_\lambda P)_{V,e}/(\rho c^2)$ is known as the thermicity; see [Fickett and Davis, 1979, p. 78].

Appendix C. Shock-change equation

Gradients in the flow variables behind a reactive shock can be related to the change in strength of the shock and the reaction rate. We start with the Lagrangian form of the flow equations (21b–d) and Eq. (25) substituted for the mass equation (21a). The time derivative along the front is

$$\frac{\mathsf{d}}{\mathsf{d}t_s} = \frac{\mathsf{d}}{\mathsf{d}t} + (u_s - u)\partial_x \ .$$

Substituting $\mathsf{d}/\mathsf{d}t_s$ for $\mathsf{d}/\mathsf{d}t$, the flow equations yield a system of linear equations for the flow gradients;

$$\begin{pmatrix} u_s - u & -\rho c^2 & 0 & 0 \\ -V & u_s - u & 0 & 0 \\ 0 & -PV & u_s - u & 0 \\ 0 & 0 & 0 & u_s - u \end{pmatrix} \begin{pmatrix} \partial_x P \\ \partial_x u \\ \partial_x e \\ \partial_x \lambda \end{pmatrix} = \begin{pmatrix} \frac{\mathsf{d}P}{\mathsf{d}t_s} - (\partial_\lambda P)_{V,e}\mathcal{R} \\ \frac{\mathsf{d}u}{\mathsf{d}t_s} \\ \frac{\mathsf{d}e}{\mathsf{d}t_s} \\ \frac{\mathsf{d}\lambda}{\mathsf{d}t_s} - \mathcal{R} \end{pmatrix} \ .$$

The matrix on the left hand side can be inverted to yield

$$\begin{pmatrix} \partial_x P \\ \partial_x u \\ \partial_x e \\ \partial_x \lambda \end{pmatrix} = \begin{pmatrix} -\frac{u_s-u}{w^2} & -\frac{\rho c^2}{w^2} & 0 & 0 \\ -\frac{V}{w^2} & -\frac{u_s-u}{w^2} & 0 & 0 \\ \frac{-PV^2}{(u_s-u)w^2} & -\frac{PV}{w^2} & \frac{1}{u_s-u} & 0 \\ 0 & 0 & 0 & \frac{1}{u_s-u} \end{pmatrix} \begin{pmatrix} \frac{\mathsf{d}P}{\mathsf{d}t_s} - (\partial_\lambda P)_{V,e}\mathcal{R} \\ \frac{\mathsf{d}u}{\mathsf{d}t_s} \\ \frac{\mathsf{d}e}{\mathsf{d}t_s} \\ \frac{\mathsf{d}\lambda}{\mathsf{d}t_s} - \mathcal{R} \end{pmatrix} , \qquad (27)$$

where $w^2 = c^2 - (u_s - u)^2$.

For a shock-to-detonation transition, the time derivatives at the shock front are determined by the Pop plot and the reactive Hugoniot. There are 4 equations for 5 unknowns; 4 gradients and the rate. Hence the Forest fire model requires an additional assumption to determine the rate. For the original derivation [Mader and Forest, 1976], the assumption is that $\partial_x P = 0$. In this case, the first element of Eq. (27) gives

$$(\partial_\lambda P)\mathcal{R} = \frac{\mathsf{d}P}{\mathsf{d}t_s} + \frac{\rho c^2}{u_s - u}\frac{\mathsf{d}u}{\mathsf{d}t_s} \ .$$

This is equivalent to the characteristic equation (10) with $\frac{\mathsf{d}u}{\mathsf{d}t}$ set to zero. In fact, with $\partial_x P = -\rho\frac{\mathsf{d}u}{\mathsf{d}t}$, the first element of Eq. (27) is equivalent to Eq. (10).

References

T. D. Aslam, J. B. Bdzil, and D. S. Stewart. Level set methods applied to modelling detonation shock dynmaics. *J. Comp. Phys.*, 126:390–409, 1996.

M. R. Baer, C. A. Hall, R. L. Gustavesen, D. E. Hooks, S. A. Sheffield, and G. T. Sutherland. Isentropic compression studies of the mesoscale response of energetic composites and constitutents. In *Thirteenth Symposium (International) on Detonation*, 2006. URL `http://www.intdetsymp.org/detsymp2006/downloadmanuscript.asp`, IDS003.

J. B. Bdzil and W. C. Davis. Time-dependent detonations. Technical Report LA-5926-MS, Los Alamos Scientific Laboratory, 1975. URL `http://lib-www.lanl.gov/cgi-bin/getfile?00316164.pdf`.

J. B. Bdzil and D. S. Stewart. Modelling two-dimensional detonations with detonation shock dynamics. *Phys. Fluids A*, 1:1261–1267, 1989.

A. W. Campbell, W. C. Davis, J. B. Ramsay, and J. R. Travis. Shock initiation of solid explosives. *Phys. Fluids*, 4:511–521, 1961a.

A. W. Campbell, W. C. Davis, and J. R. Travis. Shock initiation of detonation in liquid explosives. *Phys. Fluids*, 4:498–510, 1961b.

A. W. Campbell and R. Engelke. The diameter effect in high-density herogeneous explosives. In *Sixth Symposium (International) on Detonation*, pages 642–652, 1976.

A. W. Campbell and J. R. Travis. The shock desensitization of PBX-9404 and composition B-3. In *Eighth Symposium (International) on Detonation*, pages 1057–1068, 1986.

P. Colella, A. Majda, and V. Roytburd. Theoretical and numerical structure for reacting shock waves. *SIAM J. Sci. Stat. Comput.*, 7:1059–1080, 1986.

D. DeOliveria, A. K. Kapila, D. W. Schwendeman, J. B. Bdzil, W. D. Henshaw, and C. M. Tarver. Detonation diffraction, dead zones and the ignition and growth model. In *Thirteenth Symposium (International) on Detonation*, 2006. URL `http://www.intdetsymp.org/detsymp2006/downloadmanuscript.asp`, IDS080.

J. J. Dick. Buildup to detonation in solid high explosives during plane shock initiation: some comparisons. In *Eighteenth Symposium (International) on Combustion*, pages 1623–1629, 1981.

J. J. Dick, C. A. Forest, J. B. Ramsay, and W. L. Seitz. The Hugoniot and shock sensitivity of a plastic-bonded TATB explosive PBX 9502. *J. Appl. Phys.*, 63:4881–4888, 1988.

P. Donguy and N. Legrand. Numerical simulations of non-ideal detonations of a heterogeneous explosive with the two-dimensional Eulerian code C.E.E. In *Seventh Symposium (International) on Detonation*, pages 695–702, 1981.

A. P. Esposito, D. L. Farber, J. E. Reaugh, and J. M. Zaug. Reaction propagation rates in HMX at high pressure. *Propellants, Explosives, Pyroptechnics*, 28:83–88, 2003.

A. V. Fedorov. Detonation wave structure in liquid homogneous, solid heterogeneous and agatized HE. In *Twelfth (International) Symposium on Detonation*, 2002.

W. Fickett and W. C. Davis. *Detonation*. Univ. of Calif. Press, 1979.

C. A. Forest. Burning and detonation. Technical Report LA-7245, Los Alamos Scientific Laboratory, 1978. URL `http://lib-www.lanl.gov/cgi-bin/getfile?00818200.pdf`.

C. A. Forest, J. Wackerle, J. J. Dick, S. A. Sheffield, and D. R. Pettit. Lagrangian analysis of MIV gauge experiments on PBX 9502 using the mass-displacement moment function. In *Ninth Symposium (International) on Detonation*, pages 683–692, 1989.

J. N. Fritz, R. S. Hixson, M. S. Shaw, C. E. Morris, and R. G. McQueen. Overdriven-detonation and sound-speed measurements in PBX 9501 and the thermodynamic Chapman-Jouguet pressure. *J. Appl. Phys.*, 80:6129–6149, 1996.

I. Gasser and P. Szmolyan. A geometric singular perturbation analysis of detonation and deflagraion waves. *SIAM J. Math. Anal.*, 24:968–986, 1993.

T. R. Gibbs and A. Popolato, editors. *LASL Explosive Property Data*. Univ. of Calif. Press, 1980. URL `http://lib-www.lanl.gov/ladcdmp/epro.pdf`.

W. A. Goddard, D. I. Meiron, M. Ortiz, J. E. Shepherd, and J. Pool. Annual technical report. Technical Report 032, Center for Simulation of Dynamic Response in Materials, Calif. Inst. of Tech., 1998. URL `http://www.cacr.caltech.edu/ASAP/publications/cit-asci-tr/cit-asci-tr032.pdf`.

R. L. Gustavsen, S. A. Sheffield, and R. R. Alcon. Detonation wave profiles in HMX based explosives. In *Shock Compression of Condensed Matter – 1997*, pages 739–742, 1998a.

R. L. Gustavsen, S. A. Sheffield, and R. R. Alcon. Progress in measuring detonation wave profiles in PBX 9501. In *Eleventh (International) Symposium on Detonation*, 1998b.

R. L. Gustavsen, S. A. Sheffield, R. R. Alcon, and L. G. Hill. Shock initiation of new and aged PBX 9501 measured with embedded electromagnetic particle velocity gauges. Technical Report LA-13634-MS, Los Alamos National Laboratory, 1999. URL `http://lib-www.lanl.gov/cgi-bin/getfile?00416767.pdf`.

L. G. Hill and R. L. Gustavsen. On the characterization and mechanisms of shock initiation in heterogeneous explosives. In *Twelfth (International) Symposium on Detonation*, page 975, 2002.

R. S. Hixson, M. S. Shaw, J. N. Fritz, J. N. Vorthman, and W. W. Anderson. Release isentropes of overdriven plastic-bonded explosive PBX 9501. *J. Appl. Phys.*, 88:6287–6293, 2000.

D. E. Hooks, D. B. Hayes, D. E. Hare, D. B. Reisman, K. S. Vandersall, J. W. Forbes, and C. A. Hall. Isentropic compression of cyclotetramethylene tetranitramine HMX single crystals to 50 GPa. *J. Appl. Phys.*, 99:124901, 2006.

J. N. Johnson, P. K. Tang, and C. A. Forest. Shock-wave initiation of heterogeneous reactive solids. *J. Appl. Phys.*, 57:4323–4334, 1985.

D. E. Lambert, D. S. Stewart, S. Yoo, and B. L. Wescott. Experimental validation of detonation shock dynamics in condensed explosives. *J. Fluid Mech.*, 546:227–253, 2006.

E. L. Lee and C. M. Tarver. Phenomenological model of shock initiation in heterogeneous explosives. *Phys. Fluids*, 23:2362–2372, 1980.

I. E. Linstrom. Plane shock initiation of an RDX plastic bonded explosive. *J. Appl. Phys.*, 37:4873–4880, 1966.

B. G. Loboiko and S. N. Lubyatinsky. Reaction zones of detonating solid explosives. *Combustion Explosion and Shock Waves*, 36:716–733, 2000.

E. A. Lunstrom. Evaluation of Forest fire burn model of reaction kinetics of heterogeneous explosives. Technical Report NWC TP 6898, Naval Weapons Center, China Lake, 1988.

C. L. Mader. The two-dimensional hydrodynamic hot spot Vol. II. Technical Report LA-3235, Los Alamos Scientific laboratory, 1965. URL `http://lib-www.lanl.gov/cgi-bin/getfile?00403698.pdf`.

C. L. Mader. Empirical model of heterogeneous shock initiation of the explosive 9404. Technical Report LA-4475, Los Alamos Scientific laboratory, 1970. URL `http://lib-www.lanl.gov/cgi-bin/getfile?00378485.pdf`.

C. L. Mader. *Numerical Modeling of Explosives and Propellants*. CRC Press, second edition, 1998.

C. L. Mader and C. A. Forest. Two-dimensional homogeneous and heterogeneous detonation wave propagation. Technical Report LA-6259, Los Alamos Scientific Laboratory, 1976. URL `http://lib-www.lanl.gov/cgi-bin/getfile?00322771.pdf`.

C. L. Mader, J. D. Zumbro, and E. N. Ferm. Proton radiograpic and numerical modeling of colliding diverging PBX-9502 detonations. In *Twelve Symposium (International) on Detonation*, 2002. URL `http://www.intdetsymp.org/detsymp2002/PaperSubmit/FinalManuscript/pdf/Mader-32.pdf`.

R. Menikoff. Pore collapse and hot spots in HMX. In *Shock Compression of Condensed Matter – 2003*, pages 393–396, 2004.

R. Menikoff. Detonation waves in PBX 9501. *Combustion Theory and Modelling*, 10:1003–1021, 2006.

R. Menikoff. Empirical equations of state for solids. In Y. Horie, editor, *Solids I*, volume 2 of *Shock Wave Science and Technology Reference Library*, chapter 4. Springer-Verlag, 2007.

R. Menikoff, K. S. Lackner, and B. G. Bukiet. Modeling flows with curved detonation waves. *Combustion and Flame*, 104:219–240, 1996.

R. Menikoff and T. D. Sewell. Complete equation of state for beta-HMX and implications for initiation. In *Shock Compression of Condensed Matter – 2003*, pages 157–160, 2004.

I. Plaksin, J. Campos, P. Simões, A. Portugal, J. Ribeiro, R. Mendes, and J. Góis. Detonation study of energetic micro-samples. In *Twelve Symposium (International) on Detonation*, 2002. URL `http://www.intdetsymp.org/detsymp2002/PaperSubmit/FinalManuscript/pdf/Plaksin-094.PDF`.

J. B. Ramsay and A. Popolato. Analysis of shock wave and initiation data for solid explosives. In *Fourth Symposium (International) on Detonation*, pages 29–35, 1965.

M. S. Shaw, 2004. private communication.

M. S. Shaw and G. K. Straub. HYDROX : a one-dimensional Lagrangian hydrodynamics code. Technical Report LA-8642-M, Los Alamos Scientific laboratory, 1981. URL `http://lib-www.lanl.gov/cgi-bin/getfile?00307055.pdf`.

S. A. Sheffield, R. L. Gustavsen, R. R. Alcon, D. L. Robbins, and D. B. Stahl. High pressure Hugoniot and reaction rate measurements in PBX 9501. In *Shock Compression of Condensed Matter – 2003*, pages 1033–1036, 2004.

P. C. Souers, H. G. Andreski, C. F. Cook, R. Garza, R. Pastrone, D. Phillips, F. Roeske, P. Vitello, and J. D. Molitoris. LX-17 corner-turning. *Propellants, Explosives, Pyrotechnics*, 29:359–367, 2004.

J. Starkenberg. An assessment of the performance of the original and modified versions of the Forest fire explosive initiaion model. In *Tenth Symposium (International) on Detonation*, pages 992–1002, 1993.

J. Starkenberg, D. E. Kooker, and L. Tran. The performance of explosive shock-initiation models under complex shock loading. In *Thirteenth Symposium (International) on Detonation*, 2006. URL `http://www.intdetsymp.org/detsymp2006/downloadmanuscript.asp`, IDS130.

G. B. Whitham. *Linear and Nonlinear Waves*. Wiley, 1974.